JGR Planets

RESEARCH ARTICLE
10.1029/2021JE007080

This article is a companion to Griffin et al. (2022), https://doi.org/10.1029/2021JE007082.

Key Points:

- S-type to LS-type crystallographic preferred orientation (CPO) identified in the nakhlites
- CPO indicate nakhlite formation in environments characteristic of crystal settling
- CPO and emplacement modeling suggest random variation in discharge through time with overarching consistent emplacement

Supporting Information:

Supporting Information may be found in the online version of this article.

Correspondence to:

S. Griffin,
Sammy.Griffin@glasgow.ac.uk

Citation:

Griffin, S., Daly, L., Keller, T., Piazolo, S., Forman, L. V., Lee, M. R., et al. (2022). Constraints on the emplacement of Martian nakhlite igneous rocks and their source volcano from advanced micro-petrofabric analysis. *Journal of Geophysical Research: Planets*, *127*, e2021JE007080. https://doi.org/10.1029/2021JE007080

Received 2 OCT 2021
Accepted 10 MAY 2022

Author Contributions:

Conceptualization: S. Griffin, L. Daly, T. Keller
Data curation: S. Griffin
Formal analysis: S. Griffin, L. V. Forman, R. J. Baumgartner, P. W. Trimby, G. K. Benedix
Funding acquisition: M. R. Lee
Investigation: S. Griffin
Methodology: S. Griffin, T. Keller
Project Administration: M. R. Lee
Resources: L. V. Forman, M. R. Lee, G. K. Benedix, A. J. Irving, B. Hoefnagels

Constraints on the Emplacement of Martian Nakhlite Igneous Rocks and Their Source Volcano From Advanced Micro-Petrofabric Analysis

S. Griffin[1], L. Daly[1,2,3,4], T. Keller[1], S. Piazolo[5], L. V. Forman[2,6], M. R. Lee[1], R. J. Baumgartner[7,8], P. W. Trimby[9], G. K. Benedix[2,6,10], A. J. Irving[11], and B. Hoefnagels[12]

[1]School of Geographical and Earth Sciences, University of Glasgow, Glasgow, UK, [2]Space Science and Technology Centre, School of Earth and Planetary Sciences, Curtin University, Perth, WA, Australia, [3]Australian Centre for Microscopy and Microanalysis, The University of Sydney, Sydney, NSW, Australia, [4]Department of Materials, University of Oxford, Oxford, UK, [5]School of Earth and Environment, University of Leeds, Leeds, UK, [6]Department of Earth and Planetary Sciences, Western Australia Museum, Perth, WA, Australia, [7]School of Biological, Earth and Environmental Sciences, The University of New South Wales, Kensington, NSW, Australia, [8]CSIRO Mineral Resources, Australian Resources Research Centre, Kensington, WA, Australia, [9]Oxford Instruments Nano Analysis, High Wycombe, UK, [10]Planetary Sciences Institute, Tucson, AZ, USA, [11]Department of Earth and Space Sciences, University of Washington, Seattle, WA, USA, [12]Big Bang Meteorites

Abstract The Martian nakhlite meteorites, which represent multiple events that belong to a single magma source region represent a key opportunity to study the evolution of Martian petrogenesis. Here 16 of the 26 identified nakhlite specimens are studied using coupled electron backscatter diffraction (EBSD) and emplacement end-member calculations. EBSD was used to determine shape preferred orientation of contained augite (high Ca-clinopyroxene) phenocrysts by considering their crystallographic preferred orientation (CPO). Parameters derived from EBSD, and energy dispersive X-ray spectroscopy spectra were used in basic emplacement models to assess their dominant mechanism against three end-member scenarios: thermal diffusion, crystal settling, and crystal convection. Results from CPO analyses indicate low intensity weak-moderate CPO. In all samples, a consistent foliation within the <001> axes of augite are observed typically coupled with a weaker lineation CPO in one of the other crystallographic axes. These CPO results agree best with crystal settling being the dominant emplacement mechanism for the nakhlites. Modeled crystal settling results identify two distinguishable groups outside of the model's resolution indicating the presence of secondary emplacement mechanisms. Comparison of the two identified groups against CPO, geochemical, and age parameters indicate random variability between individual meteorites. Therefore, coupled CPO and emplacement modeling results identify an overarching characteristic of a dominant crystal settling emplacement mechanism for the nakhlite source volcano despite exhibiting random variation with each discharge through time.

Plain Language Summary A group of Martian meteorites known as the nakhlites was investigated to better understand volcanism on Mars by using the specialist microscopy technique of electron backscatter diffraction and basic modeling of known igneous processes. The presented data suggest that the magma that was discharged from the nakhlite source volcano varied randomly through time but solidified into rocks via a consistent dominant mechanism of crystal settling. These findings show Martian volcanism is dynamic, where individual eruptions are variable, yet retain overarching volcanic source characteristics that can be identified from large studies of multiple samples.

1. Introduction

Mars is a planet whose landscape has been created to a large degree by igneous processes (Carr & Head, 2010; Greeley & Spudis, 1981; Grott et al., 2013; Taylor, 2013) and modified by hypervelocity impacts (Carr & Head, 2010; Zuber, 2001). From remote sensing studies of the volcanic provinces present on Mars, it is clear that volcanism on the planet has been long lived, spanning several billions of years (Lapen et al., 2010, 2017; Werner, 2009). Despite orbital monitoring since 1964, observation of active Martian volcanism has not yet occured. Despite the wealth of knowledge gained from remotely analyzing Martian volcanoes, there is a limit to our understanding of the magmatic processes on Mars that can be gained from remote sensing alone (e.g., constraints on interior volcanic processes, magma chamber evolution, quantitative assessment of magma composition, determination

Supervision: L. Daly, T. Keller, M. R. Lee
Visualization: S. Griffin
Writing – original draft: S. Griffin
Writing – review & editing: S. Griffin, L. Daly, S. Piazolo, M. R. Lee, R. J. Baumgartner, A. J. Irving

of physical parameters such as emplacement micro-structures and compositional variability) that can only be achieved through the analysis of physical specimens.

The Martian meteorites are the only Martian materials currently available for laboratory-based examination (McSween & Treiman, 1998; Udry et al., 2020). These samples encompass a range of different Martian rocks (e.g., the various types of shergottites, nakhlites, chassignites, an orthopyroxenite, and polymict breccias) that are interpreted to have been ejected from at least 11 different sites on Mars, most likely in the southern highlands (Udry et al., 2020). However, despite being able to group these samples chemically, isotopically, and using micro-structures including shape preferred orientation (SPO), the location of any ejection sites on Mars, their source volcano(es), and their emplacement style (e.g., flow/intrusion, sub-aerial/hypabyssal) remain unknown. Knowing how these meteorites were emplaced (flows vs. intrusions) can provide information relevant to locating their launch crater on Mars. Identifying patterns in emplacement mechanisms can provide information about whether through volcanic activity, the Martian crust (as sampled by these meteorites) has the potential to act as heat source capable of generating and sustaining liquid water on timescales relevant to create habitable regions for the development and sustenance of life (Kurokawa et al., 2014; McSween et al., 2001).

The nakhlites are currently the largest group of Martian meteorites derived from a singular parental magma source, interpreted to be a single volcano on Mars (Udry et al., 2020). At the time of this publication, there are 27 cataloged specimens representing at least four distinct magmatic events spanning 93 Ma (1,416 ± 7 to 1,322 ± 10 Ma; Cohen et al., 2017). Classed as basalts, the nakhlites are the only group of igneous rocks, with the exception of Allan Hills 84001, to contain evidence Martian fluid/rock interaction (Lee et al., 2018; Treiman, 2005). However, it is unknown whether the nakhlites sample a volcanic source which had a regular eruption record or a history consisting of longer dormant phases with condensed bursts of magmatic activity, and whether the meteorites originated solely as surficial flows, only intrusions, or as a combination of the two.

Despite geochemical and isotopic data being excellent at identifying magmatic sources, distinguishing between individual lava flows derived from a single volcano or volcanic province can be difficult where there is little chemical or mineralogical variation between units. The exception is where additional information is obtained through micro-structural analysis, geochronological data, or geological context (Fenton et al., 2004). Micro-structural and SPO properties of an igneous rock record the physical processes of a magmatic event from source to emplacement (Jerram et al., 2018). Thus, micro-structural and SPO analysis of multiple magmatic units derived from a single magmatic source can provide important information regarding its evolution and historical processes.

Recent electron backscatter diffraction (EBSD) crystallographic preferred orientation (CPO) measurements on the nakhlite meteorites Governador Valadares, Lafayette, Miller Range (MIL) 03346, and Nakhla by Daly, Piazolo, et al. (2019) showed evidence for gravitational (i.e., crystal) settling in all four samples. Weak flow CPO was also identified in Governador Valadares and Nakhla, indicating potential complex petrogenesis within the nakhlite launch site. Daly, Piazolo, et al. (2019) hypothesized at least three distinct magmatic systems encompassing two regimes (subaerial hyperbolic flow and crystal settling) are represented within the nakhlites. Here, we use EBSD data to substantially expand on this work, assessing CPO formed during emplacement and generating input parameters to calculate magmatic body end-member emplacement mechanisms via calculated unit thicknesses for 16 known nakhlite meteorite stones. The acquired data were then used to investigate what variation and/or trends can be discerned to better understand whether the hypothesized diversity of magmatic systems within the nakhlites proposed by Daly, Piazolo, et al. (2019) are applicable across an expanded nakhlite suite or to just a few individual samples.

2. Materials and Methods

2.1. Electron Backscatter Diffraction

EBSD analysis used a combination of premade and newly made polished thick sections of the nakhlites (21 sections encompassing 16 individual stones; Table 1). The samples were chosen to capture the growing diversity

of the nakhlite suite considering the recovery location, known crystallization age, and modal mineralogy. All sections were cut with random orientations that is, without respect to any known/inferred SPO and/or CPO. To ensure comparability and consistency between the different datasets, EBSD map's principal orientations are defined as follows: X = left-right map direction, Y = top-bottom map direction, and Z = direction perpendicular to the map plane. Data used in our analyses include previously presented EBSD datasets which can be found in Daly, Lee, et al. (2019), Daly, Piazolo, et al. (2019), and Lee et al. (2018).

Prior to EBSD analysis, all sections were mechanically and chemically polished. Mechanical polishing was undertaken using 1 μm and then 0.3 μm aluminum spheres suspended in glycol for 5 min each. Subsequent chemical polishing was achieved using 0.1 μm colloidal silica suspended in a NaOH solution for 4 hrs. Following polishing, a ~10 nm thick conductive carbon coat was deposited in all specimens using a sputter coater.

Coupled EBSD and energy dispersive X-ray spectroscopy (EDS) analysis was run on four different instruments: a Zeiss Sigma Field Emission Gun Variable Pressure Scanning Electron Microscope (FEG-VP-SEM) operating Oxford Instruments AZtec analysis software v3.3 (ISAAC Imaging Centre, University of Glasgow); a Carl Zeiss EVO SEM using a HKL NordlysNano high Sensitivity EBSD detector (Geochemical Analysis Unit [GAU], Macquarie University), a Hitachi SU70 FEG-SEM equipped with a Symmetry CMOS detector and indexed using Aztec analysis software v3.4 (Oxford Instruments NanoAnalysis HQ, High Wycombe), and a Tescan MIRA3 VP-FEG-SEM with the NordlysNano EBSD detector and Aztec EDS/EBSD acquisition system (John de Laeter Centre, Curtin University). All analyses were run at 20 KeV, 4–8 nA beam current, 20 keV, 70° tilt, aperture of 120 μm, under high vacuum (~3.5×10^{-4} Pa) apart from Lafayette and MIL 03346, which were run at low vacuum (~49 Pa). Selected step sizes for each sample were chosen to maximize the area covered by the EBSD maps and ensure data collection over available timeframes. The detailed analysis settings for each analyzed section, including step sizes (ranging from 2 to 15 μm), are in Table 1.

All data were processed using Oxford Instruments HKL Channel 5 software. Noise reduction was done using a wildspike correction followed by a consecutive 8–6 point nearest neighbor zero solution reduction to facilitate crystal definition without generating significant artifacts within the data set and to remove erroneous, mis-indexed and non-indexed, data points (Bestmann & Prior, 2003; Forman et al., 2016). From the cleaned data set grain orientation spread (GOS) and maximum orientation spread from the mean grain orientation (MOS) values were ascertained. Note that the cleaning of the data set impacts the reported values by lowering the spread of orientations (Ruzicka & Hugo, 2018). The noise-reduced data were then further processed through the one point per grain (OPPG; i.e., one point per crystal) reduction scheme, where excess points resulted from fractured crystals were manually removed from the data set prior to CPO and SPO analysis. Crystals containing <10 pixels and measuring <20 μm^2 in were also removed from the data set as they contained too few datapoints to robustly identify crystal's phase, based on the scan resolution, step size, and shock levels within the sample (Forman et al., 2019; Watt et al., 2006). Crystal grain boundaries (defined as >10° internal crystallographic misorientation from the nearest-neighbor pixel) within the datasets were determined using HKL Channel 5's automated "grain detect" algorithm. These crystal boundaries were further processed to exclude twin boundaries (180° rotation) identified to occur along augite's <100>, <001>, <204>, or <104> axes. Thus, HKL Channel 5 derived crystal lists can be used to interpret and quantify CPO within the different scans. GOS and MOS were also calculated using HKL Channel 5 taking into account twin boundaries, fractured crystals, and stitched map boundaries. To assess CPO three different quantitative metrics J-Index, M-Index, and Eigenvalues (PGR) were compared together. All three metrics assess the orientation distribution function (ODF) of the crystals in a slightly different manner: J-Index uses the Euler angles (Bunge, 1982), M-Index assesses the crystal axes with equal weighting (Skemer et al., 2005), and Eigenvalues assess the ODF of each crystallographic axis individually between three end-members (Vollmer, 1990). For calculating the quantitative metrics and providing crystal statistics for thickness calculations raw files in *.ctf* (common transfer file) format were imported into MTEX. In MTEX the data underwent denoising (equivalent to HKL Channel 5's wildspike), before establishing 10° misorientation as the crystal boundary and identifying twin crystals. The detected crystals were then separated into two groups; crystals <200 μm were classed as mesostasis crystals, and crystals ≥200 μm were classed as phenocryst crystals.

Table 1
Nakhlite Electron Backscatter Diffraction Analysis Settings

	Caleta el Cobre 022	Governador Valadares		Lafayette	MIL 03346	MIL 090030	MIL 090032	MIL 090136	Nakhla	
	CERGE	BM.1975, M16, P8469	BM.1975, M16, P19783	USNM 1505-5	118	50	108	62	WAM 12965	USNM 426-1
Area (mm^2)	112.83	15.48	21.03	73.56	106.4	79.64	14.69	43.17	13.3	209.57
Pixel Count	16,430,075	1,719,852	93456	1,659,474	6,653,595	8,848,637	1,631,700	3,606,066	59450	23,285,660
Hit Rate (%)	100	55.53	90.98	1,659,474	59.1	100	69.62	28.66	75.29	50.05
Section analyzed	Partial	Whole	Partial	Partial	Partial	Partial	Partial	Partial	Partial	Partial
Step size (μm)	3	3	15	4	4	3	3	3	15	3
Tilt (°)	70	70	70	70	70	70	70	70	70	70
Accelerating voltage (keV)	20	20	20	20	20	20	20	20	20	20
Aperture (μm)	120	120	120	120	120	120	120	120	120	120
Beam Exposure (ms/EBSP)	24	28	30–40	30–40	30–40	21	26	24	30–40	28
Beam Current (nA)	21	4.1	8	4.1	4.1	21	4.1	4.1	8	21
Total (all phases)										
MAD	0.74	0.6	0.48	0.59	0.59	0.76	0.61	0.68	0.78	0.82
Mean BS	42.32	62.35	92.01	62.87	59.1	34.01	64.8	75.01	93.82	33.96
Mean BC	58.11	81.53	119.04	78.31	72.65	61.32	68.88	55.39	118.87	53.94
Augite										
MAD	0.76	0.56	0.48	0.65	0.59	0.8	0.65	0.68	0.78	0.82
Mean BS	43.64	69.44	91.9	56.31	58.53	32.91	62.33	74.89	93.39	33.76
Mean BC	57.42	90.5	118.90	66.54	71.14	58.1	65.15	54.96	118.05	53.17
Forsterite										
MAD	0.67	0.47	0.43	0.52	0.65	0.73	0.58	0.74	0.76	0.83
Mean BS	44.88	87.37	111.57	68.64	54.61	33.9	62.89	84.76	0.12	34.4
Mean BC	65.21	122.53	142.80	88.4	64.31	58.56	64.84	74.02	0.49	53.4
Bin criteria	4 × 4	4 × 4	4 × 4	4 × 4	4 × 4	1 × 1	4 × 4	4 × 4	4 × 4	4 × 4
EDS collected	Yes	Yes	Yes	Yes	Yes	Yes	Yes	Yes	Yes	Yes
Additional EDS map	Yes	No	No	No	No	Yes	Yes	Yes	No	No
Collected	CU	UofG	MU	UofG	UofG	CU	UofG	UofG	MU	CU

Note. EBSP = electron backscatter patterns a.k.a. Kikuchi diffraction patterns; CU = Curtin University; MAD = mean angular deviation; MU = Macquarie University; BS = band slope; UofG = University of Glasgow; BC = back contrast; OIN = Oxford Instruments NanoAnalysis, High Wycombe; EDS = electron dispersive spectroscopy.

2.2. Shape Preferred Orientation

SPO represents the orientation relationships of the crystals within a given sample. The study of Daly, Piazolo, et al. (2019) showed that a coupling exists in augite between the long shape-axis and <001>, also referred to as the <*c*> crystallographic axes, within the nakhlites Governador Valadares, Lafayette, MIL 03346, Nakhla. Correlation between the long shape-axis and <001> was also assessed and confirmed for all analyzed samples in this study. Thus, for SPO analysis, the slope of the crystallographic <001> axes of the reduced OPPG subset is used as a proxy for the long shape-axis within the sections to assess the 3D corrected SPO. The oriented crystals from the reduced OPPG datasets provides consistency across the multiple specimens analyzed, removes bias

NWA 817	NWA 998		NWA 10153	NWA 11013	NWA 12542	Y 000593		Y 000749		Y 000802
N8-1	T1	UG-1	SH65 T-2, 2	UG-1	F83-1	106-A	127-A	64-A	72-A	36-A
7.6	9.86	36.14	37.01	37.01	113.65	36.09	23.78	64.56	48.92	35.86
47,493,378	1,578,314	1,784,876	12,537,585	5,921,530	12,627,810	4,010,028	2,183,888	5,928,192	5,546,892	1,434,422
42.37	56.4	55.57	59.15	46.36	76.81	66.71	69.04	48.88	31.68	73.16
Partial	Whole	Partial	Partial	Partial	Partial	Whole	Partial	Partial	Whole	Partial
0.4	2.5	4.5	3	2.5	3	3	3.5	3.5	3	5
70	70	70	70	70	70	70	70	70	70	70
15	20	20	20	20	20	20	20	20	20	20
120	120	120	120	120	120	120	120	120	120	120
	24	26	25	32	25	29	26	26	30	24
12	4.1	4.1	18	4.1	4.1	4.1	4.1	4.1	4.1	4.1
0.56	0.69	0.7	0.82	0.69	0.57	0.67	0.55	0.73	0.66	0.66
104.81	50.68	0.08	39.19	52.65	68.86	51.54	87.91	50.35	68.97	53.4
96.77	57.46	0.38	47.71	62.47	82.56	62.34	98.45	51.79	78.05	65.8
0.56	0.71	0.71	0.84	0.69	0.56	0.65	0.54	0.75	0.66	0.69
104.81	50.67	48.54	40.27	51.67	70.93	54.4	88.99	48.7	68.17	50.43
96.77	57.12	55.68	47.86	60.58	84.12	67.97	99.3	48.26	76.64	59.57
0.57	0.62	0.6	0.78	0.6	0.49	0.7	0.46	0.64	0.69	0.57
106.54	56.6	56.8	40.04	61.95	73.62	52.06	104.42	54.87	72.89	58.69
98.05	71.25	73.69	49.18	81.24	91.23	60.85	122.29	61.92	85.03	77.04
4 × 4	4 × 4	4 × 4	4 × 4	4 × 4	4 × 4	4 × 4	4 × 4	4 × 4	4 × 4	4 × 4
Yes	Yes	Yes	Yes	Yes	Yes	Yes	Yes	Yes	Yes	Yes
No	No	No	No	No	Yes	No	Yes	Yes	No	Yes
OIN	UofG	UofG	CU	UofG	UofG	UofG	UofG	UofG	UofG	UofG

against the lack of geological context or unknown sample orientation (e.g., Figure 1), as well as bias from crystal fracturing within each section. The trace of the crystallographic axes was calculated using the slope angle of Oxford Instruments' HKL Channel 5 Tango module best-fit ellipse algorithm, which was also used to calculate crystal area and length of the long shape-axis.

2.3. Crystallographic Preferred Orientation

CPO refers to the preferred orientation of the crystallographic lattice axes for a selected phase within a sample. CPO was visually assessed from the reduced OPPG data set (accounting for fractured crystals) where one pixel/

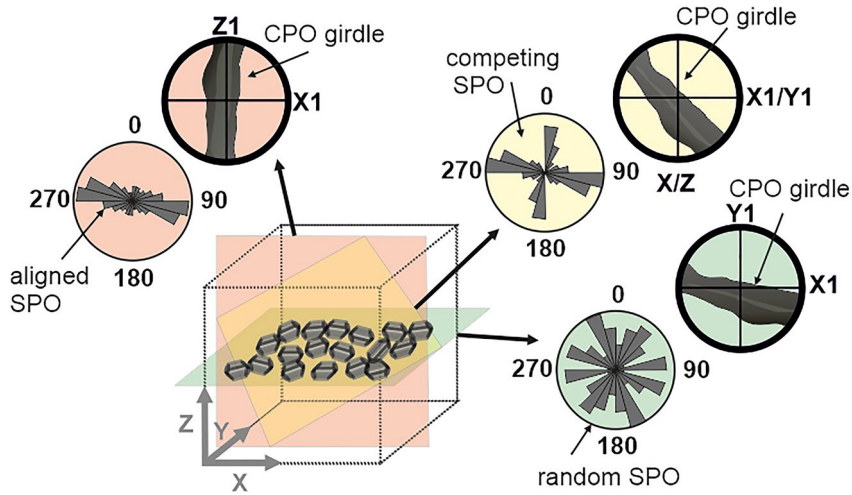

Figure 1. Example shape preferred orientation (SPO; thin outline) and crystallographic preferred orientation (CPO; thick outline) plots of a sample exhibiting crystal settling (XY plane orientation). SPO and CPO plots depict variation resulting from the analysis plane orientation (perpendicular [pink, ZX], oblique [yellow, X1||X, Y1||Z] and parallel [green, XY]) relative to crystal settling. SPO plots depicted as rose diagrams show the long axes of crystals which represent the trace of the crystal directions whereas CPO plots depicted as pole figures show the dominant crystal axes orientation corresponding to the trace of the crystal directions relative to the analysis plane (colored).

crystallographic orientation is used to define a crystal. Lower hemisphere equal area projections contoured using a maximum multiple uniform density (MUD; representing the density of data points) of 5 with 5° clustering and a half width of 15° were used to plot <100>, [010], [0–10], and <001> crystallographic axes.

CPO intensity and/or presence was quantified from the phenocryst group of crystals (≥200 μm) using an adapted MATLAB MTEX code from Daly, Piazolo, et al. (2019), adapted from Vollmer (1990) with corrections from Mainprice et al. (2015), generating J-Index, M-Index, and Eigenvalue values (Bunge, 1982; Skemer et al., 2005; Vollmer, 1990). Assessment of CPO metrics has shown comparable datasets are required for an accurate assessment where the minimum number of crystals required to produce stable metrics (~2% variation) will result in the symmetry and intensity of the CPO (Mainprice et al., 2015). For the nakhlites the minimum number of crystals to produce stable metrics was determined to be ~300. Where possible, each metric was calculated utilizing the largest 300 crystals or the entire phenocryst population (based of n_{MTEX} values; Table 2) to enable more accurate comparison between the different sized datasets.

The strength and intensity of CPO was determined using a combination of three CPO metrics, where the same comparative terrestrial equivalent parameters as stated in Daly, Piazolo, et al. (2019). Briefly, J-Index values and their associated CPO were assessed as: low = 1.40–1.80, low-medium = 1.80–3.00, medium 2.40–5.00, medium-strong = 4.00–12.00, and strong <12; M-Index: 0 = random orientation and 1 = single crystal (note that although M-Index calculations work well for many different minerals, clinopyroxene has been recognised to produce weak M-Index values irrespective of the overall classified CPO strength of the rock). Eigenvalue end-members are assessed as: random (R) = >90%, weak point (P) and girdle (G) = 10%–30%, moderate P and G = 30%–50%, and strong P and G = >50%. Eigenvalues, typically notated as λ_1, λ_2, and λ_3, assess CPO symmetry and axes orientation as a fraction between three end-members (P, G, R) where the combined PGR value for each crystallographic axis equals 1 (Mainprice et al., 2015; Vollmer, 1990). Common eigenvalue index parameters, BA and LS which assess the shape relationship of the Eigenvalue CPO between perpendicular crystallographic axes were calculated using the following equations:

$$\mathrm{BA} = \frac{1}{2}\left[2 - \left(\frac{P_{010}}{G_{010} + P_{010}}\right) - \left(\frac{G_{100}}{G_{100} + P_{100}}\right)\right] \quad (1)$$

$$\mathrm{LS} = \frac{1}{2}\left[2 - \left(\frac{P_{010}}{G_{010} + P_{010}}\right) - \left(\frac{G_{001}}{G_{001} + P_{001}}\right)\right] \quad (2)$$

These index parameters result in a number ranging 0–1. The BA-Index (Equation 1) assesses the shape between a pure <100> girdle Eigenvalue ("A"-type foliation = 0) and a pure <010> point Eigenvalue ("B"-type lineation = 1). The LS-Index (Equation 2) assesses the shape between a pure <001> girdle Eigenvalue ("S"-type foliation = 0) and a pure <010> point Eigenvalue ("L"-type lineation = 1).

2.4. Calculating Magma Body Thicknesses Used to Indicate Feasibility of Dominant End-Member Emplacement Mechanism

Approximate magma body thicknesses (D) for each data set, used to indicate feasibility of three dominant end-member emplacement mechanisms for the nakhlites, were calculated using MATLAB with MTEX toolbox (Bachmann et al., 2011). These three equations of thermal diffusion (Equation 3), crystal settling (Equation 4), and crystal convection (Equation 5) were selected as they represent processes that result in the maximum possible thickness, intermediary thickness, and minimum thickness, respectively, of a given magmatic unit:

$$D_{\text{diff}} = \sqrt{\kappa T} \tag{3}$$

$$D_{\text{sett}} = (1-\theta)^4 \frac{\Delta\rho}{\mu} g a^2 T \tag{4}$$

$$D_{\text{conv}} = \frac{\mu}{T\theta\Delta\rho g}. \tag{5}$$

In Equation 3, κ is the thermal diffusivity of basalt (7.5×10^{-7} m/s; Durham et al., 1987). In Equations 3–5, T is the residence time taken from (Krämer Ruggiu et al., 2020; Udry & Day, 2018). In Equations 4 and 5, θ is the crystal volume fraction (from EBSD data derived by dividing the total area occupied by phenocrysts [all phases] by the total map area), $\Delta\rho$ is the density difference between the melt and solid lava (calculated from CIPW normative EDS spectra), g is the Martian gravity, a is the crystal diameter (from MTEX calculated phenocryst grouped crystal), and μ is the viscosity (calculated from CIPW normative EDS spectra).

To calculate CIPW normative spectra, large area spectra encompassing the EDS map areas were collected. The collected spectra was then processed following standard CIPW normative procedures (Bickel, 1979; Pruseth, 2009). The CIPW normative results were then used to calculate different model input parameters such as density and viscosity. Liquid magma temperatures used for density and viscosity estimates were calculated using the linear equation of McBirney (1993), which bases temperature from silica content within the sample. These estimated temperatures ranged between 1043°C and 1121°C (for CIPW results, full code, and input parameters see Supporting Information S1).

3. Results

3.1. Modal Mineralogy and Augite Morphology

The EBSD scans of the nakhlites show a wide range of phenocrysts (c, i.e., crystals ≥0.2 mm), mesostasis material (ms, i.e., crystals <0.2 mm), and non-indexed phases (ni; consisting of glass, fractures/holes, or amorphous phases; Figures 2 and 3). Overall, deviations (σ) of ±0.15 (c), 0.11 (ms), and 0.13 (ni) vol.%, respectfully are observed across the datasets. Governador Valadares exhibits the highest proportion of phenocrysts (averaging 40 vol.%), Caleta el Cobre 022 the highest proportion of mesostasis material (60 vol.%), and Y 000749 the highest proportion of non-indexed phases (averaging 61 vol.%). All samples have augite as the dominant phase (62 vol.% in Y 000802 to 32 vol.% in NWA 817), followed by olivine (12 vol.% for averaged Y 000593 to 0.3 vol.% in NWA 11013) and lesser percentages of plagioclase (9 vol.% in Caleta el Cobre 022 to 0 vol.% e.g., MIL 03346), titanomagnetite (1.7 vol.% in NWA 12542 to 0.1 vol.% in MIL 090136), and alteration products (0.9 vol.% in NWA 817 and 0.1 vol.% e.g., NWA 10153) (Figure 3). The modal mineralogy determined agrees with previously reported values sitting within the know 40% variability range for a given nakhlite (Corrigan et al., 2015). Replicate sections sourced from the same meteorite show that variations in the ratio of crystallinity:mesostasis material:non-indexed are well below the variation ($\sigma \pm 0.15$) observed across the whole data set, with exception of the two Y 000593 scans ($\sigma \pm 0.3$; Figure 3).

Table 2
Nakhlite Augite Grain Statistics

		Caleta el Cobre 022	Governador Valadares		Lafayette	MIL 03346	MIL 090030	MIL 090032	MIL 090136	Nakhla	
		CERGE	BM.1975, M16, P8469	BM.1975, M16, P19783	USNM 1505-5	118	62	108	50	USNM 426-1	WAM 12965
Augite indexed (%)		46.7	40.9	79.5	52.1	58.5	45.2	55.8	43.2	44.6	66
N (all data)		48844	1,215	355	4,572	5,675	4,273	620	1,567	23824	304
N (OPPG; >200 μm)		276	93	137	156	301	210	104	267	1,093	138
N (MTEX; >200 μm)		1,789	134	326	899	984	596	126	355	2,492	234
Diameter (μm)											
Av.		86.23	37.837	204.2	57.6	59.09	48.31	65.88	69.31	34.44	148.34
SD		95.78	70.57	124.31	81.30	97.21	88.91	112.99	99.69	58.62	90.55
Aspect ratio											
A-axis											
Av.		1.83	2.65	2.12	1.87	2.05	1.85	2.09	1.75	1.8	1.66
NA		1,788	10	10	244	331	308	75	102	1,177	23
SD		0.64	2.26	0.92	0.7	0.92	0.62	1.03	0.59	0.57	0.43
B-axis											
Av.		1.83	2.17	2.09	1.92	2.13	1.71	1.94	1.66	1.76	1.14
NB		146	58	3	37	10	1	9	8	166	1
SD		0.63	0.94	0.30	0.91	0.61	n.d.	0.87	0.57	0.55	n.d.
C-axis											
Av.		1.86	2.30	2.26	1.86	1.90	1.84	1.63	1.80	1.78	1.51
NC		1,954	22	10	178	165	34	19	25	638	5
SD		0.72	1.88	1.03	0.66	0.71	0.61	0.54	0.54	0.55	0.28
All axes											
Av.		1.84	2.34	1.97	1.87	2.00	1.85	2.01	1.76	1.78	1.63
NT		3,888	90	23	459	506	343	103	135	1,981	29
SD		0.69	1.71	0.77	0.69	0.86	0.31	0.97	0.58	0.55	0.41
Elongate grains (%)		7.96	7.41	6.48	10.04	8.92	8.03	16.61	8.62	8.32	9.54
GOS (°)		0.09–14.19	0.22–11.02	0.24–6.31	0.35–6.01	0.25–10.19	0.14–5.36	0.27–4.07	0.13–3.53	0.07–9.16	0.28–5.86
Av.		1.53	2.09	0.93	1.07	1.98	0.78	0.94	0.63	1.23	1.46
SD		1.14	1.68	0.86	0.77	1.36	0.39	0.46	0.31	0.79	1
MOS (°)		0.14–45.29	0.56–57.39	0.41–20.46	1.93–31.00	0.45–46.51	0.22–13.16	0.55–16.11	0.41–9.78	0.13–32.6	0.61–19.00
Av.		5.33	7.41	3.72	7.12	6.71	2.5	4.66	3.31	3.60	5.45
SD		4.51	6.16	2.93	3.94	4.74	1.96	2.9	1.37	3.06	3.34
CPO											
M-Index		0.01 ± 0.0002	0.04 ± 0.011	0.03 ± 0.010	0.01 ± 0.004	0.02 ± 0.006	0.01 ± 0.004	0.03 ± 0.009	0.02 ± 0.007	0.02 ± 0.0004	0.02 ± 0.006
J-Index		1.37 ± 0.07	4.35 ± 0.65	2.57 ± 0.13	2.27 ± 0.11	2.05 ± 0.10	2.36 ± 0.12	5.33 ± 0.80	3.14 ± 0.16	1.5 ± 0.08	2.85 ± 0.14
Eigenvalue											
Point (*P*)	<100>	0.08	0.10	0.15	0.05	0.17	0.11	0.16	0.13	0.13	0.12
	<010>	0.05	0.09	0.08	0.08	0.05	0.03	0.10	0.06	0.08	0.08
	<001>	0.05	0.14	0.13	0.07	0.03	0.01	0.15	0.08	0.01	0.04
Girdle (*G*)	<100>	0.07	0.07	0.07	0.05	0.04	0.08	0.05	0.16	0.04	0.14
	<010>	0.04	0.26	0.17	0.12	0.56	0.09	0.08	0.10	0.03	0.06
	<001>	0.27	0.37	0.42	0.29	0.45	0.31	0.21	0.33	0.48	0.47

NWA 817	NWA 998		NWA 10153	NWA 11013	NWA 12542	Y 000593		Y 000749		Y 000802
N8-1	T1	UG-1	SH65 T-2, 2	UG-1	F83-1	106-A	127-A	64-A	72-A	36-A
31.7	48.3	44.5	42.8	44.4	59.1	54.6	53.2	44.7	29.2	62.4
4,282	998	1,888	19759	8,922	9,964	1,035	395	7,450	2,478	670
50	68	135	385	177	963	93	109	197	111	138
43	110	356	849	273	1,081	241	219	447	281	341
6.6	38.31	59.08	24.27	23.37	46.32	71.04	227.86	33.76	32.46	132.19
26.61	66.44	78.58	45.87	38.17	79.95	132.94	144.54	59.36	113.90	154.33
1.99	1.7	1.79	1.76	1.81	2.05	2.36	1.85	1.968	1.88	2.02
72	49	84	687	214	400	13	5	287	66	42
0.68	0.48	0.55	0.57	0.6	0.93	1.30	0.92	0.65	0.72	0.88
2.07	1.74	2.25	1.74	1.85	1.88	1.90	5.33	2.09	1.84	2.01
4	8	7	69	10	27	21	2	60	52	14
1.01	0.45	0.87	0.46	0.57	0.67	0.70	1.19	0.65	0.52	1.04
2.25	1.81	1.79	1.80	1.95	2.10	2.04	1.59	1.96	2.35	1.98
64	36	54	797	338	138	27	3	84	25	22
1.02	0.67	0.55	0.76	0.81	0.97	0.88	0.63	0.68	1.09	1.27
2.11	1.75	1.81	1.78	1.91	2.05	2.07	2.47	1.97	1.95	1.98
140	93	145	1,553	562	565	66	10	556	149	78
0.86	0.55	0.57	0.67	0.74	0.93	0.94	1.70	0.66	0.76	1.11
3.27	9.32	7.68	7.86	6.30	5.67	6.38	2.53	7.46	6.01	11.64
0.05–5.29	0.24–8.38	0.00–6.78	0.01–10.41	0.12–9.10	0.20–10.37	0.29–8.78	0.13–3.94	0.23–6.97	0.11–2.50	0.29–6.95
0.79	1.13	1.28	1.8	2.09	1.51	1.77	0.44	0.66	0.41	0.92
0.58	0.86	0.83	1.16	1.23	1.06	1.39	0.32	0.32	0.22	0.67
0.10–25.35	0.30–19.73	0.00–29.47	0.06–46.65	0.45–37.69	0.43–45.96	0.46–35.95	0.25–10.75	0.40–31.24	0.23–9.61	0.52–14.81
2.31	4.1	4.79	4.96	6.26	7.25	5.83	2.44	2.00	1.46	3.80
2.41	3.51	3.56	4.47	4.48	4.99	4.96	1.92	1.43	1.22	2.37
0.08 ± 0.049	0.03 ± 0.013	0.02 ± 0.007	0.01 ± 0.0003	0.02 ± 0.006	0.02 ± 0.0003	0.03 ± 0.008	0.03 ± 0.007	0.03 ± 0.009	0.04 ± 0.011	0.02 ± 0.006
14.42 ± 8.65	4.97 ± 0.74	2.78 ± 0.14	1.78 ± 0.09	3.33 ± 0.17	1.54 ± 0.08	3.41 ± 0.17	4.62 ± 0.23	2.66 ± 0.13	3.61 ± 0.18	2.67 ± 0.13
0.26	0.09	0.04	0.15	0.18	0.12	0.04	0.06	0.13	0.13	0.12
0.11	0.10	0.09	0.03	0.04	0.06	0.01	0.14	0.07	0.08	0.08
0.24	0.10	0.01	0.06	0.07	0.06	0.17	0.10	0.10	0.16	0.15
0.24	0.08	0.10	0.08	0.09	0.07	0.18	0.11	0.03	0.02	0.15
0.34	0.11	0.18	0.01	0.15	0.05	0.09	0.08	0.15	0.20	0.05
0.29	0.37	0.38	0.32	0.37	0.40	0.27	0.41	0.42	0.37	0.19

Table 2
Continued

		Caleta el Cobre 022	Governador Valadares		Lafayette	MIL 03346	MIL 090030	MIL 090032	MIL 090136	Nakhla	
		CERGE	BM.1975, M16, P8469	BM.1975, M16, P19783	USNM 1505-5	118	62	108	50	USNM 426-1	WAM 12965
Random (*R*)	<100>	0.86	0.83	0.79	0.90	0.79	0.81	0.80	0.71	0.83	0.7.9
	<010>	0.92	0.66	0.75	0.81	0.90	0.88	0.81	0.84	0.90	0.87
	<001>	0.68	0.49	0.45	0.64	0.52	0.68	0.64	0.59	0.51	0.49
LS-Index		0.31	0.51	0.46	0.40	0.30	0.38	0.43	0.42	0.16	0.25
BA-Index		0.50	0.66	0.69	0.56	0.67	0.66	0.60	0.55	0.53	0.44
MUD max-min		0.06–2.54	0.00–3.96	0.00–2.64	0.06–2.29	0.04–2.97	0.02–3.14	0.00–3.85	0.08–3.01	0.14–2.19	0.00–3.87

Note. *N* = number of grains; NA = number of grains in subset A; CPO = crystal preferred orientation; OPPG = one point per grain, accounted for fractured crystals; NB = number of grains in subset B; MUD = multiples of uniform density; Av. = average; NC = number of grains in subset C; GOS = grain orientation spread; SD = standard deviation; NT = total number of grains with any axis parallel to the plane of the sample. MOS = max deviation orientation spread from the mean grain value (see Supporting Information S1 for spreadsheet format).

3.2. Augite Phenocryst Shape Preferred Orientation

The subhedral to euhedral augite crystals exhibit coupling between the short <001> crystallographic axes and the long shape-axis (Figure 4). This enables the <001> to be used as a proxy tracer for the long shape-axis within the nakhlites. The nakhlites show a range of SPO from moderate (one dominant direction of alignment with a smaller less dominant direction, e.g., NWA 12542) to random (no alignment, e.g., NWA 11013; Figure 4). Moreover, the data show an average GOS difference of 1.2° ± 0.8°, reflecting the high proportion of low angle deviations, despite datasets exhibiting larger GOS ranges for example, 0.1°–14.2° (Caleta el Cobre 022) to 0.1°–3.5° (MIL 090136; Figure 5, Table 2). MOS values exhibit deviation ranges from 0.41 to 9.78 in MIL 090136 to 0.56–57.39 in Governador Valadares (BM1975,M16,P8469) with values averaging 4.5° ± 3.3° across all datasets (Figure 5, Table 2). Within the 21 individual datasets a small proportion of augite crystals were observed to have any of the three crystallographic axes aligned parallel (±5°) to the cut surface of the thick sections (Figure 6, Table 2). Parallel <001> axes aligned crystal values range from 3.3% in NWA 998, (T1) to 16.6% in MIL 090032 with an overall deviation of 2.9%. The reduced OPPG datasets detected crystals with <001> axes oriented ±5° parallel to the acquisition surface ranging from 0% in NWA 998, (T1) to 21% in Lafayette. These oriented crystals deviated 5.7% across the 21 individual scans. Assessing <001> oriented crystals across the complete data set an overall deviation of ±1% is observed ranging from 0.8% in Y 000593 (127-A) to 4% in NWA 10153. The proportion of aligned elongate crystals (i.e., with at least one crystallographic axis oriented parallel [±5°] to the analysis plane) ranges from 2.5% to 10.0% (Y 000593 [127-A] and Lafayette, respectively; Figure 6, Table 2).

3.3. Crystallographic Preferred Orientation

CPO is variable across the set of analyzed nakhlite specimens. All meteorites show low intensity, weak-moderate girdle CPO within the <001>, which becomes more defined against the MUD contouring with increased crystal count (Figure 4). The lowest MUD range appears within section Y 000749 (64-A; 0.46–0.22). The largest MUD range is observed within NWA 817 (0.00–4.68). However, the position of the girdle in sample MIL 090030 makes the feature harder to discern (Figure 4, for the complete set of pole figures see Figure A3 in Supporting Information S1). To calculate quantitative metrics, the number of crystals were also detected within MTEX. Augite crystals identified using MTEX's grain detection algorithm reported as n_{MTEX} range from 43 crystals (NWA 817) to 2,492 crystals (Nakhla [USNM 426-1]; Table 2). Twelve of these datasets contain <300 crystals, resulting in higher errors for all CPO calculations. Out of the 12 smaller datasets only NWA 817 contained <100 crystals (Table 2). Thus, despite including data for NWA 817 in this study, the results are not discussed and interpreted owing to the large associated error (e.g., Figure 7).

Quantitative metrics of CPO calculated using MTEX show low M-Index values, ranging from 0.01 ± 0.0002–0.004 (Caleta el Cobre 022, Lafayette, and MIL 090030) to 0.04 ± 0.011 (Y 000749 [72-A] and Governador Vala-

NWA 817	NWA 998		NWA 10153	NWA 11013	NWA 12542	Y 000593		Y 000749		Y 000802
N8-1	T1	UG-1	SH65 T-2, 2	UG-1	F83-1	106-A	127-A	64-A	72-A	36-A
0.50	0.83	0.86	0.77	0.74	0.81	0.78	0.83	0.90	0.87	0.73
0.55	0.79	0.73	0.96	0.81	0.90	0.78	0.78	0.72	0.72	0.87
0.47	0.53	0.62	0.63	0.56	0.54	0.56	0.49	0.46	0.50	0.65
0.60	0.37	0.35	0.23	0.48	0.28	0.38	0.29	0.44	0.54	0.41
0.64	0.53	0.50	0.48	0.73	0.54	0.27	0.37	0.74	0.79	0.42
0.00–4.68	0.00–4.42	0.00–3.23	0.08–2.52	0.02–4.00	0.03–2.37	0.23–5.92	0.26–2.91	0.46–2.22	0.22–4.78	0.59–2.26

dares, [both sections]), with a significant proportion of the data showing M-Index values around 0.02 (Figure 7, Table 2). J-Index values are observed to range from 1.37 ± 0.07 (Caleta el Cobre 022) to 4.97 ± 0.74 (NWA 998, T1; Table 2) giving an average J-Index value of 2.96 ± 1.12; this value places the nakhlites in the medium strength CPO range (Figure 7). Resulting PGR values from Eigenvalue analysis support low intensity CPO which range in CPO strength. Calculated CPO intensity in the analyzed nakhlites ranged from 0.25 (Caleta el Cobre 022, MIL 090030) to 0.75 (Nakhla [WAM 12695], Y 000749 [72-A]) indicating weak intensity for all samples. Identified girdle strengths for <001> range from weak (0.19 in Y 000802) to medium (0.48 in Nakhla [USNM 426-1]) (Figure 8, Table 2), where 15 of the 21 sections exhibited low intensity medium strength <001> girdle CPO. Low intensity (≤0.4) weak point <100> are also present in a large portion of the samples ranging in strength from 0.10 to 0.18 (Figure 8). Samples Caleta el Cobre 022, Lafayette, NWA 998 (UG-1 only), and Y 000593 (both sections) exhibited random point <100> values (Figure 8). MIL 090032, and NWA 998 (T1 only) exhibited weak point values for point CPO in both <100> (0.15 and 0.26, respectively) and <010> axes (0.10, Figure 8). Both replicate sections of Y 000593 exhibited low intensity (~0.3) weak point <010> values (0.13) (Figure 8, Table 2). Lafayette and Y 000749 (Section 72-A only) exhibit random <100> values (0.90) and Caleta el Cobre 022 and NWA 10153 scans exhibit random <010> values (0.92 and 0.96, respectively; Figure 8, Table 2). The majority of the sections exhibit S to LS-type CPO (Figure 9, Table 2) with LS indices ranging from 0.16 in Nakhla (USNM 426-1) to 0.54 in Y 000749 (72-A). BA indices range from 0.27 in Y 000593 (106-A) to 0.79 in Y 000749 (72-A), with 16 of the sections indicating stronger point <010> over girdle <100> (Figure 9, Table 2).

3.4. Calculated Magma Body Thicknesses Used to Assess Feasibility of Dominant Emplacement Mechanism

Calculated thicknesses for the individual nakhlites reported here are preliminary and are intended to serve as general indicators that can direct future modeling work. Results are intended to determine the most viable emplacement mechanism for the nakhlites, rather than exact unit thicknesses. Due to the resolution of the current calculations, reported results are only able to be discussed in terms of magnitude scale (i.e., centimeter, meter, vs., tens of meters).

For a thermal diffusion emplacement mechanism (Equation 3), calculated magma body thicknesses (within error) were found to sit within the tens of meters scale (Table 3). For a crystal settling emplacement mechanism (Equation 4), magma body thicknesses were calculated to span several different orders of magnitude that outside of error can be placed into two distinguishable groups <10 m (11 sections) and >10 m (10 sections; Table 3). Lastly, the calculations for the crystal convection emplacement mechanism (Equation 5), provided unrealistic thickness values in the range of tens to hundreds of nanometers indicating that the residence times used would need to reflect a single convection cycle rather than the timespan of emplacement for pure convection to be the dominant mechanism of emplacement (Table 3). The thicknesses as calculated via Equations 3–5

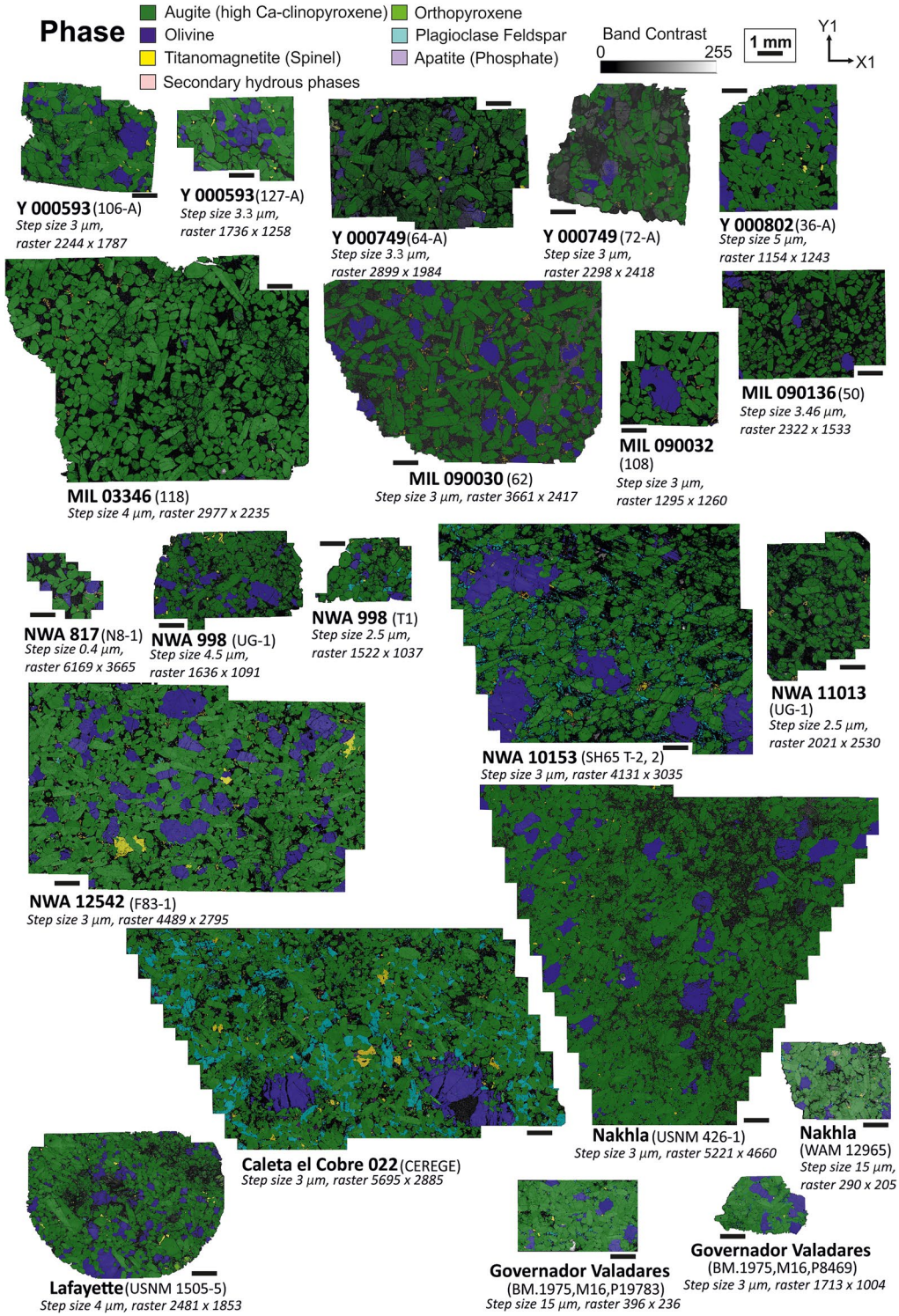

Figure 2. Electron backscatter diffraction phase maps showing the characteristic mineralogy of the nakhlite meteorites, consisting of augite (high Ca-clinopyroxene; dark green) and lesser olivine (indexed as forsterite; dark blue) together with minor orthopyroxene (indexed as enstatite; light green), iron-titanium oxide (indexed as titanomagnetite; yellow), and plagioclase feldspar (indexed as albite; light blue). Note the high proportion of plagioclase mesostasis material in the Caleta el Cobre 022 meteorite compared to the other nakhlites studied here.

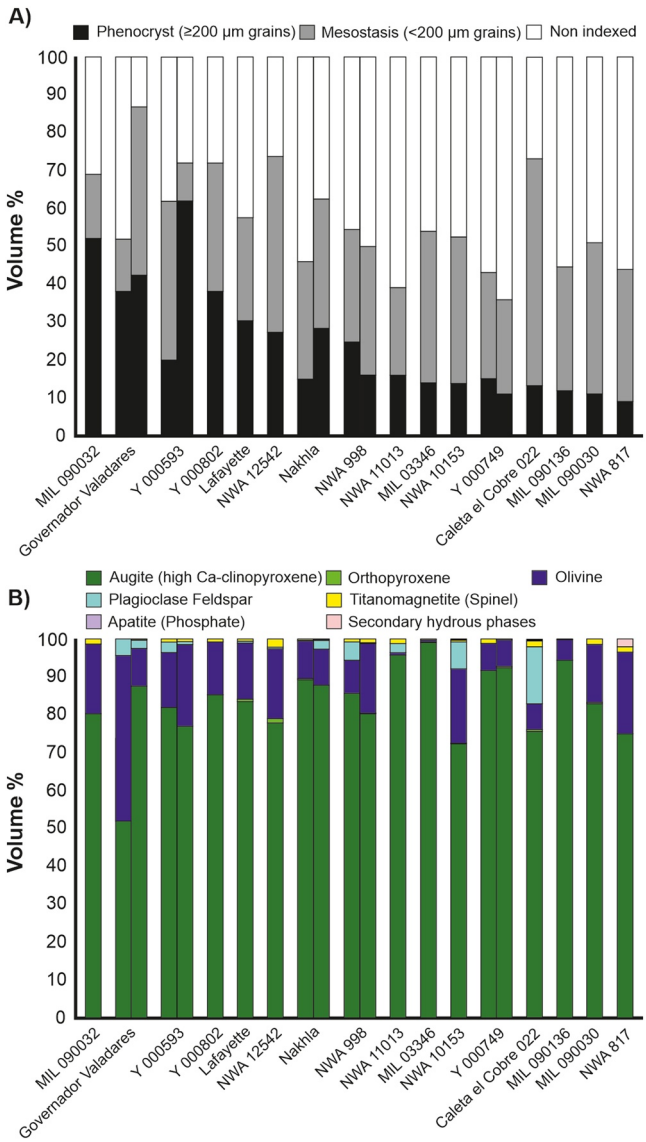

Figure 3. Modal mineralogy of the nakhlites from electron backscatter diffraction (EBSD) data. (a) Area percent of phenocrysts (≥200 µm crystals), mesostasis material (<200 µm crystals), and non-indexed material (mainly glass and fractures but can also consist of holes and amorphous material). (b) Area percent of all indexed phases in EBSD data that is, this is for both phenocryst and mesostasis phases. (See Supporting Information S1 for data in table version).

are very different to each other, the reasons for these differences are further evaluated in section 4.2. No correlations could be discerned when comparing calculated magma body thicknesses against modeling input parameters (e.g., Figure 10), observed CPO metrics (e.g., Figure 11), or available published geochemistry or age parameters.

4. Discussion

4.1. Nakhlite CPO Observations

Orientation relationship observations, here defined as the geometric associations between the sample's constituent crystals, provide insights into important petrological processes such as crystallization growth rates, magma mixing, emplacement mechanisms, etc. Specifically, EBSD provides 3D orientation information for crystals analyzed within the 2D sample analysis plane (thin or thick petrologic section) through the relationships between crystallographic and shape axes. This information is important for the study of meteorites derived from large achondritic bodies, such as the Martian nakhlites, where gravitational forces undoubtedly influenced crystallization but the original orientation of the meteorites is unknown (Daly, Piazolo, et al., 2019).

Previous EBSD studies of a limited set of nakhlite meteorites provide a baseline for understanding crystallization processes on the basis of detected SPO and CPO of earliest crystallized—and gravitationally settled—mineral phases, particularly augite (Daly, Piazolo, et al., 2019). Data in the present study were acquired on a much larger set of nakhlites (16 specimens, Figure 4), confirm these observations, that is, augite in each of the analyzed samples shows a coupling of the <001> axes, to the long shape-axis.

In general, clinopyroxenes (i.e., augite investigated in this study) will typically exhibit weaker CPO strengths than other associated minerals (e.g., orthorhombic olivine and orthopyroxene) particularly in intrusive samples (Hidas et al., 2019; Van Der Werf et al., 2017). For augite, the combination of its euhedral shape with its monoclinic symmetry will impact observed CPO strengths. Thus, when using quantitative metrics to assess CPO strength, the overall relationship between a given crystal's shape and symmetry needs to be considered to properly contextualize the results.

4.1.1. CPO Strength From the M-Index

The M-Index values, which span a range of 0.03 (Figures 7 and 11a), indicate that the analyzed nakhlites have random CPO. Note, however, that M-Index is commonly applied in the study of olivine and other orthorhombic minerals but not monoclinic clinopyroxenes, mainly because consideration of the latter alone can provide either erroneously low CPO strength estimates or even nonsensical values even in rocks with moderate CPO strengths (e.g., Hidas et al., 2019). The M-Index determines CPO strength through assessing the degree of rotation required for two crystals to become crystallographically aligned. To achieve this, the M-Index utilizes a subset of the overall ODF spherical harmonic (Mainprice et al., 2015; Skemer et al., 2005). Among all the nakhlites studied here, a significant proportion of the augite crystals exhibit simple twins (180° rotations; Figure 6). Note, however, that a current limitation of the used MTEX code is the inability to remove twinning orientation discrepancy within crystals of lower order symmetry such as monoclinic augite. In other words, simple twins impact the M-Index calculations by underestimating true CPO strengths. The values that are observed sit in a similar range to reported ultramafic rocks on Earth (Hidas et al., 2019; Van Der Werf et al., 2017), although clinopyroxene is not the dominant phase in these studies. For the analyzed sections, the

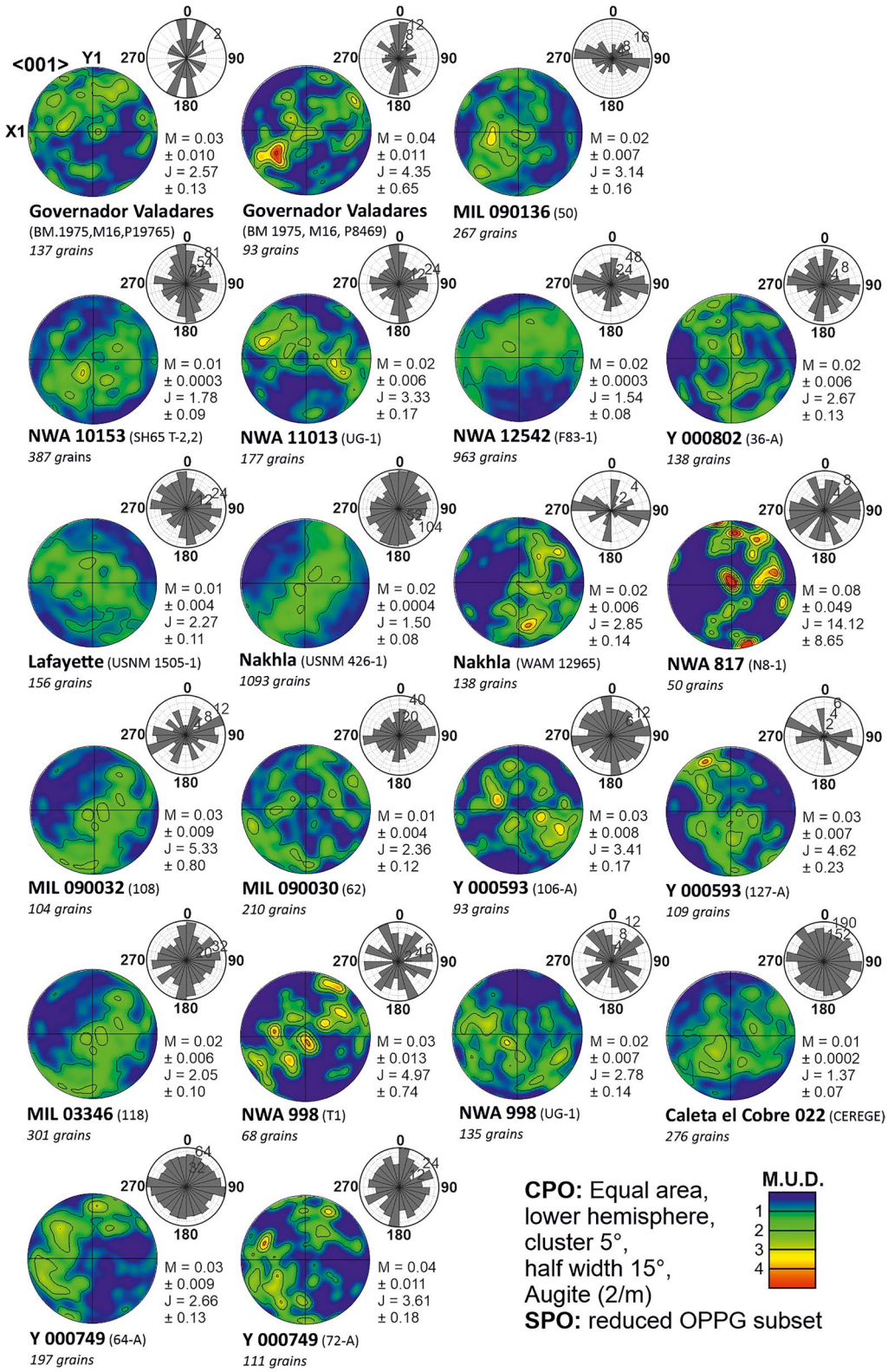

Figure 4.

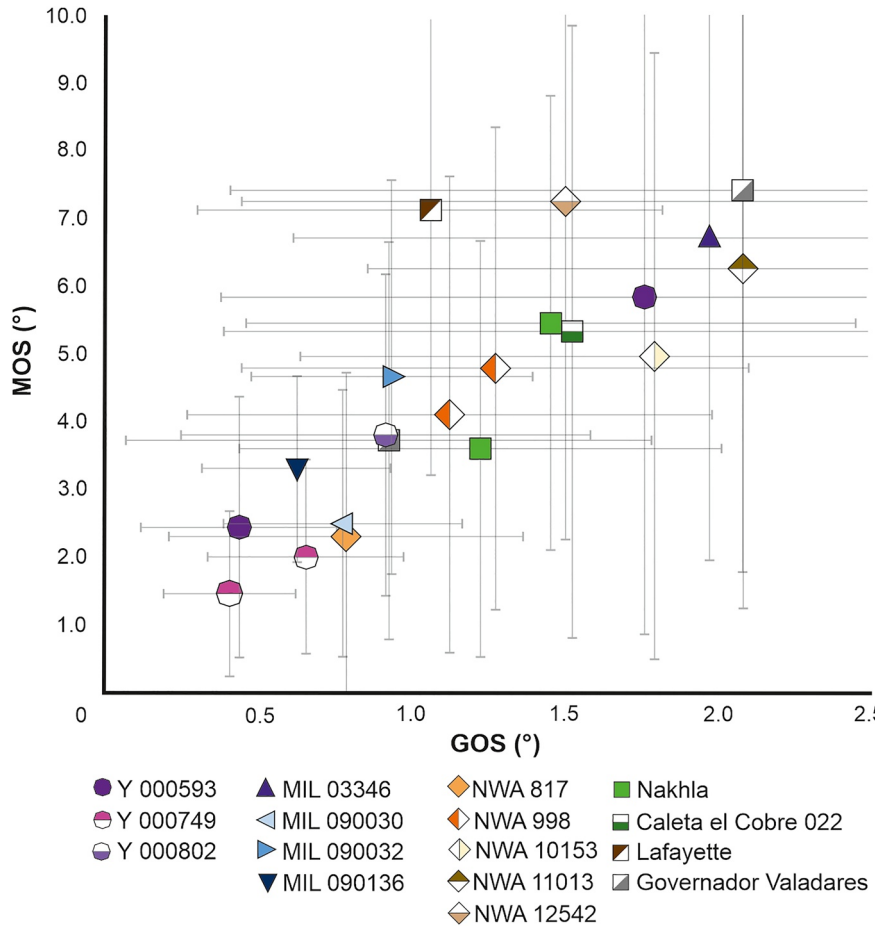

Figure 5. Average grain (i.e., crystal) orientation spread (GOS) versus average maximum orientation spread from the mean orientation value (MOS) of augite phenocrysts (≥200 μm) of analyzed nakhlites.

CPO strength from M-Index calculations is at odds with the estimates from the CPO plots but does agree with the observed SPO (Figure 4).

4.1.2. CPO Strength From the J-Index

The J-Index values indicate different CPO strengths across the across the nakhlite suite, ranging from borderline random-weak CPO to medium strength CPO (Figures 7 and 11a, Table 2). These results are consistent with data from intrusive fine-grained clinopyroxenites and coarser grained websterites on Earth (Frets et al., 2012; Henry et al., 2017). The results also indicate CPO diversity within the nakhlite's emplacement environment. However, variation in CPO within a singular magmatic body (flow and/or intrusion) is common within igneous rocks, particularly those that formed in convecting flow regimes (Lofgren, 1983; Marsh, 2013; Perugini et al., 2003).

4.1.3. CPO Shape and Strength From Eigenvalue Analysis

PGR analysis shows a consistent yet variable low intensity <001> girdle CPO, that is, <*c*> foliation as the dominant CPO across all 21 analyzed nakhlite sections (Figures 4, 8 and 11d). Girdle CPO is defined here as the alignment of one or two crystal axes along a singular plane, also known as magmatic foliation (Paterson

Figure 4. Representation of augite phenocrysts (≥200 μm) crystal preferred orientation (CPO) in the <001> axis shown on a pole figure, and shape preferred orientation (SPO) shown on a rose diagram oriented in the plane of analysis. CPO girdle features are observed within all samples. SPO plots show near random orientation in nine sections (e.g., Y 000749 [64-A and 72-A] and NWA 998 [T1]), and two main orientations also in nine sections (e.g., Nakhla [WAM 12965] and NWA 998 [UG-1]). Only three sections show aligned SPO with one dominant orientation (samples Governador Valadares [BM1975,M16,P19765 and BM1975,M16,P8469] and MIL 090136). All crystallographic data depicts the reduced one point per grain (OPPG) data set (Table 2) where additional crystallites from fractured crystals have been manually removed (Figures 1 and 2).

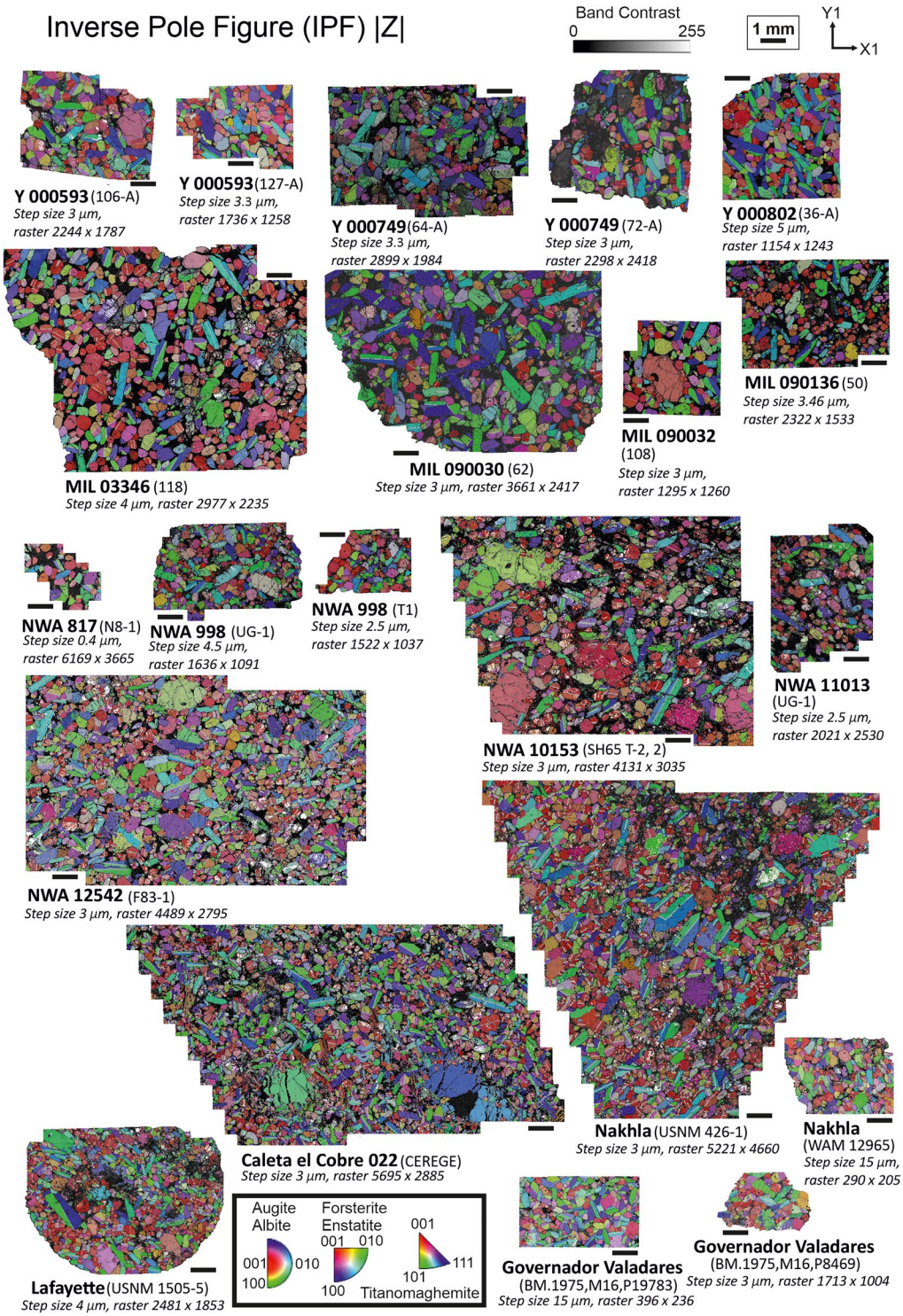

Figure 6. Inverse pole figure (IPF) |z| maps of the nakhlites. The samples show simple twinning (black) and mechanical twinning (white), predominantly within crystals of augite (high Ca-clinopyroxene). There appears to be a slight alignment of augite along its [001] axis, despite crystal orientation appearing for the most part random in nature when considering all the different phases.

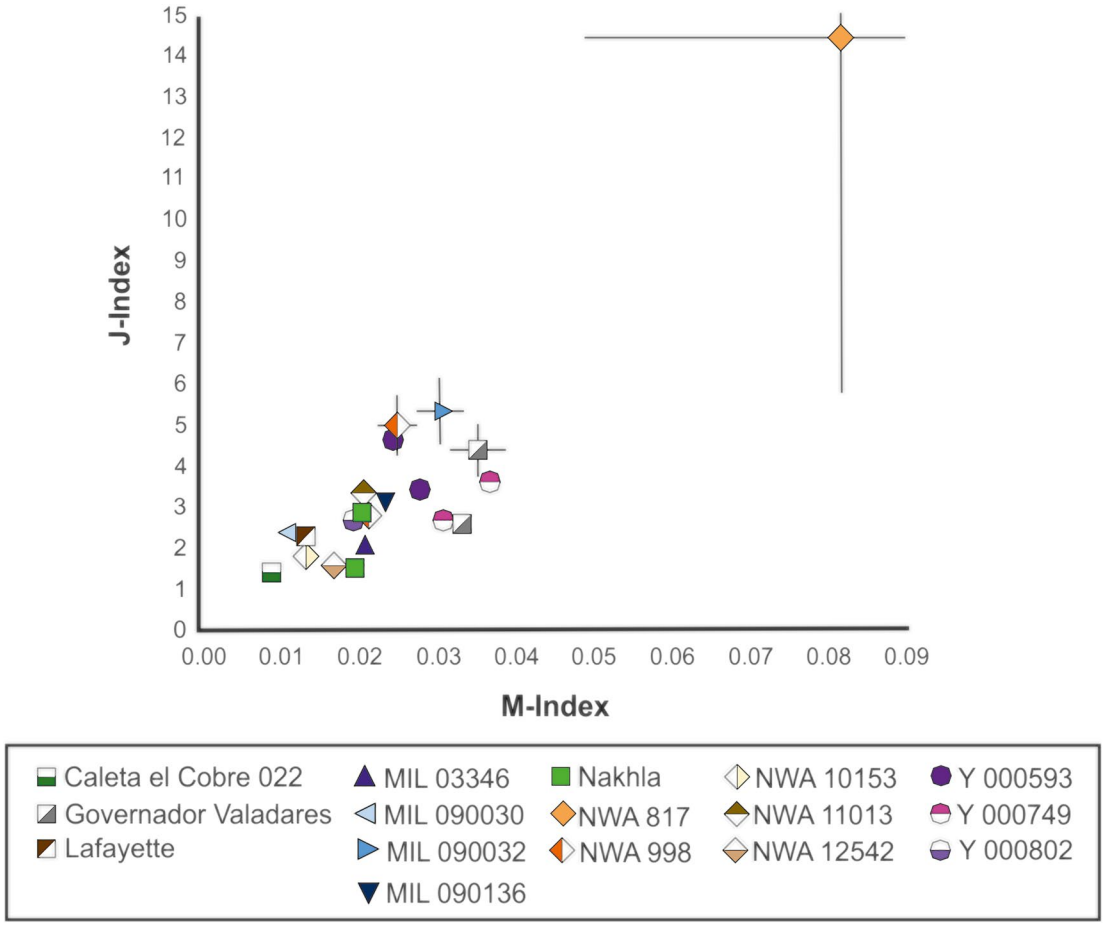

Figure 7. M-Index and J-Index values for the nakhlites. Caleta el Cobre 022 exhibits the lowest J-Index and M-Index values, while the highest observed J-Index and M-Index values, for NWA 817, are interpreted to be a function of the smaller data set size (n_{MTEX} = 43 crystals).

et al., 1998). In addition to the more dominant <001> girdle CPO, almost all sections (exempting Caleta el Cobre 022 and Lafayette) exhibit very weak-weak intensity point CPO within either <100> or <010>, that is, <*a*> and <*b*> axes, respectively (Figures 4, 8, 9 and 11). Point CPO is defined as the consistent alignment of given crystallographic axes along a singular direction also known as magmatic lineation (Paterson et al., 1998). Finally, some sections show PGR values within the <100> and <010> axes which indicate a combination of weak point with weaker <100> girdle CPO (Figures 8, 9 and 11c).

4.1.4. Intra-Sample Variability

To assess CPO variability within individual nakhlite stones two sections from each of five different meteorites were analyzed (Governador Valadares, Nakhla, NWA 998, Y 000593, and Y 000749). Previous work assessing modal mineralogy variation between replicate nakhlite sections (i.e., sections sourced from the same meteorite) showed up to 40% variation (Corrigan et al., 2015). Significant changes in modal composition will impact the expression of SPO and CPO, particularly within igneous rocks. Higher levels of mesostasis material will, in general, enable easier mobility of phenocryst crystals, whilst highly crystalline solids will allow less movement (Nicolas, 1992; Piazolo et al., 2002). The calculated standard deviation between replicate sections' quantitative CPO metrics were highest for J-Index (0.75 ± 0.13), followed by PGR (0.022 ± 0.002), then M-Index (0.02 ± 0.08; Table 2). The M-Index and J-Index standard deviations sit within the same CPO strength groupings (weak, moderate *etc.*) but are often outside of the metrics associated calculation error. The PGR values sit qualitatively within the same regions (Figure 8), however, quantitatively they do not overlap (Table 2). Both M-Index and J-Index calculations are highly dependent on the ODF. A sample's ODF represents the variability in crystal orientation relative to the analysis plane. Crystal orientation used in ODF is calculated using the Euler density,

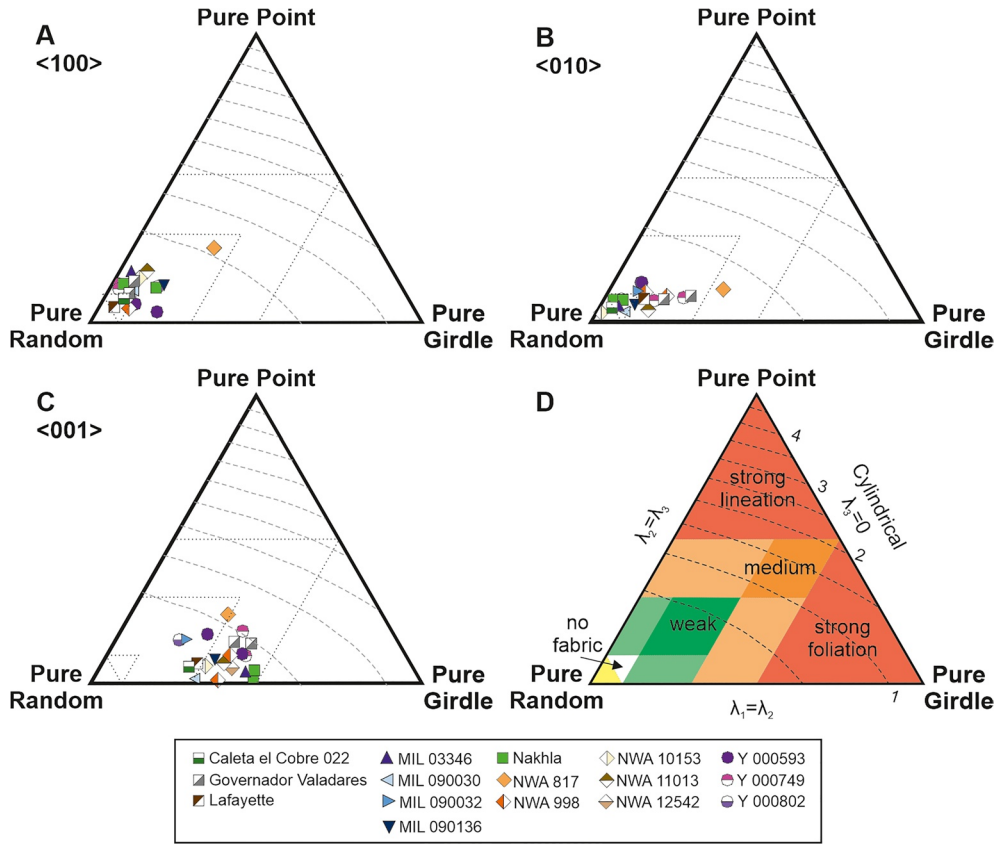

Figure 8. Eigenvalue (PGR) ternary plots of the nakhlites. (a) <100> axis showing low intensity weak point (i.e., lineation) to no CPO. (b) <010> axis shows low intensity random to weak point CPO. (c) <001> axis showing low intensity weak to moderate girdle strengths of contained crystals (corresponding to the long shape-axis), with some samples also exhibiting weak point CPO. (d) Eigenvalue PGR key. Dashed lines indicate CPO intensity, where lower intensity indicates higher levels of symmetry within the fabric. Dotted lines indicate CPO strength relative to the three endmembers. λ_1, λ_2, and λ_3 refer to the specific Eigenvalues that combine to form discussed PGR endmembers.

which is derived from the crystal's symmetry. Calculation of an accurate ODF is highly dependent on the associated halfwidth (selected as 15° for all samples in this study), which if not properly considered can distort the Euler space and bias the results (Gerth & Schwarzer, 1993; Kalidindi et al., 2009). Variable sized datasets and failure to properly accommodate fractured crystals can further influence CPO calculations. However, the third CPO metric, Eigenvalue analysis (PGR), does not rely on ODF. Instead, the PGR metric utilizes the direct Euler angle of the crystal with respect to its Miller reference frame (which for augite is <100>, <010>, and <001>). The orientation deviation of each crystal relative to the overall sample is then normalized. This normalized orientation is then assessed as a fractional component (i.e., using one Miller reference frame) between three endmembers (*P*, *G*, and *R*). This is distinctly different to the two end-member scale used for both M-Index and J-Index, which both consider a crystal in its entirety.

Across the replicate sections the main variable that could have affected the resulting CPO values is the discrepancy in the number of detected crystals. Assessment of the compositional breakdown between phenocryst, mesostasis material, and non-indexed space within the samples (Figure 2) showed the largest deviations between all three components in Y 000593 (±21 [*c*], ±16 [ms], and ±5 [ni]) and the smallest deviation within in Y 000749 (±2 [*c*], ±1.5 [ms], and ±3.5 [ni]). In terms of vol.% augite within the samples, deviation within the replicate samples is observed to range from ±0.7 (Y 000593) to ±19.3 (Governador Valadares). Placing the replicate section CPO metric deviations within the context of augite's variable abundance within each section helps to explain the observed differences in metric results outside of analytical uncertainty. It also reinforces the importance of heterogeneity in crystal distribution to the development and variation of observable CPO and SPO within a given

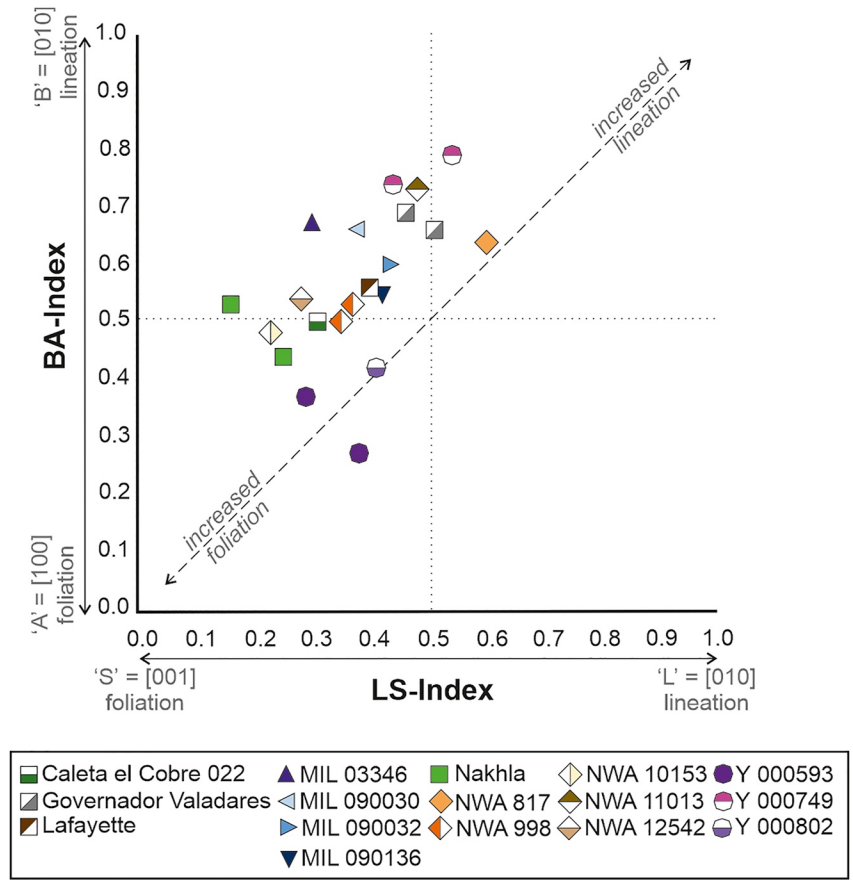

Figure 9. BA-Index versus LS-Index for the nakhlites. BA-Index assesses the shape relationship where 0 indicates a dominant girdle <100> foliation signature (A) and 1 indicates a dominant point <010> lineation signature (B; Equation 1). LS-Index assesses the shape relationship where 0 indicates a dominant girdle <001> foliation signature (S) and 1 indicates a dominant point <010> lineation signature (L; Equation 2). The nakhlites exhibit S type-LS type CPO with B type-BA-type CPO, exempting Y 000593 which exhibits S and BA-A type CPO.

sample. More importantly, in lieu of assessment of CPO from datasets containing representative numbers of crystals, analysis of multiple replicate sections can provide an increased understanding on how the CPO metric is influenced by the inherent heterogeneity of the sample. The impact on CPO calculation variability in the number of augite crystals was minimized through setting the identified 300 minimum crystal requirement as the upper limit for all datasets (affecting 12 datasets). The gold standard for number of crystals required for CPO studies is intensity dependent, where samples exhibiting lower intensity CPO, such as the nakhlites require larger datasets than samples exhibiting higher CPO (Ismaïl & Mainprice, 1998; Skemer et al., 2005). The requirement for larger crystal datasets to assess CPO can be impractical and potentially problematic for many planetary studies, where often the material available is severely limited and the amount of sample per section is generally a fraction of the size typically found in a traditional petrological section. Additionally, determination of the lower ideal crystal limit will require datasets with larger amounts of crystals. If the ideal range were to be applied to the presented nakhlite datasets, only 12 of the 21 datasets using n_{MTEX} (four datasets using n_{OPPG}; Table 2) would produce viable CPO values (i.e., with 2% error margins). Thus, CPO metrics should only be used as crude indicators, particularly in the study of scarce meteorites.

4.1.5. CPO Related to Calculated Dominant Emplacement End-Member Mechanisms

The bulk volume of an igneous body can have a significant impact on the external strain field's CPO expression within an igneous sample (Marsh, 2013). Specifically, a specimen that forms in a large flow/intrusion within which crystals are convecting (producing localized strain fields with at least two major strain directions within a

Table 3
Calculated Unit Thicknesses Based on End-Member Mechanisms Used to Assess Feasibility of Dominant Emplacement for the Nakhlites

		Unit thickness scale		
Nakhlite	Section	Thermal diffusion	Crystal settling	Crystal convection
Caleta el Cobre 022	CERGE	10s m	>10 m	n.v.
Governador Valadares	BM.1975,M16, P8469	10s m	>10 m	n.v.
	BM.1975,M16, P19783	10s m	>10 m	n.v.
Lafayette	USNM 1505-5	10s m	>10 m	n.v.
MIL 03346	118	10s m	>10 m	n.v.
MIL 090030	62	10s m	>10 m	n.v.
MIL 090032	108	10s m	>10 m	n.v.
MIL 090136	50	10s m	>10 m	n.v.
Nakhla	USNM 426-1	10s m	<10 m	n.v.
	WAM 12965	10s m	<10 m	n.v.
NWA 817	N8-1	10s m	>10 m	n.v.
NWA 998	T1	10s m	<10 m	n.v.
	UG-1	10s m	<10 m	n.v.
NWA 10153	SH65 T-2,2	10s m	<10 m	n.v.
NWA 11013	UG-1	10s m	<10 m	n.v.
NWA 12542	F83-1	10s m	>10 m	n.v.
Y 000593	106-A	10s m	<10 m	n.v.
	127-A	10s m	<10 m	n.v.
Y 000749	64-A	10s m	<10 m	n.v.
	72-A	10s m	<10 m	n.v.
Y 000802	36-A	10s m	<10 m	n.v.

Note. n.v. = non valid result. See Supporting Information S1 for spreadsheet format.

larger strain field) would be expected to exhibit a stronger CPO. The strength of this CPO would also vary more throughout the igneous body than would be found for a sample formed from either crystal settling (one dominant strain field *a.k.a.* gravity) or thermal diffusion (no strain field; Callot and Guichet [2003], Marsh [2013], and Nicolas [1992]). However, the convection end-member model calculation of Equation 5, which was intended to provide the absolute minimum potential magma body thickness, resulted in unit thicknesses that are significantly below the measured average crystal size (Tables 2 and 3). Thus, results from Equation 5 do not support a pure crystal convection mechanism as the dominant emplacement mechanism for the nakhlites. However, calculated magma body unit thicknesses for the other two mechanisms require crystal convection to also be present as a secondary mechanism. Particularly for the crystal settling calculated >10 m unit thicknesses in order to satisfy fundamental physics. If, however, crystal convection was the overriding emplacement mechanism for the nakhlites, then the residence times used in our calculations would have to represent a single round of convection rather than representing the entire crystallization process in order to produce viable results. Out of the three emplacement end-members modelled for the nakhlites, crystal settling agrees best with the observed CPO data to be the dominant emplacement mechanism (Figures 4 and 8) and moreover, produces the largest range of magma body thicknesses distinguishable as two separate groups (>10 and <10 m, Figures 10 and 11, Table 3). The identification of two distinct groups outside of error indicate that that if crystal settling is the overriding dominant emplacement for the nakhlites, then different proportions of both crystal convection and thermal diffusion are contributing to the observed CPO as secondary mechanisms. This contribution will result in different unit thicknesses than presented here in this paper.

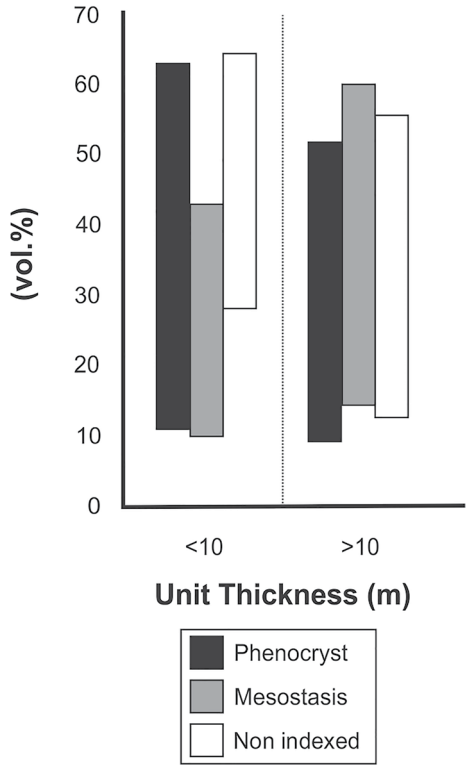

Figure 10. Identified groups based on calculated unit thicknesses (D_{sett}, Equation 4) assuming crystal settling as the dominant mechanism influencing crystal orientation versus modal variability within analyzed nakhlites. Phenocryst (≥200 μm), mesostasis (<200 μm), and non-indexed (glass, non-indexed phases, and fractures/holes).

4.2. Magmatic Emplacement Style of the Nakhlites From CPO

The observed moderate low intensity <001> foliation (Figures 4, 8, 9 and 11, Table 2) indicates a dominant shear or flattening flow regime, commonly observed in cumulate-type igneous rocks (Hunter, 1996; Iezzi & Ventura, 2002; Merle, 1998). Only Caleta el Cobre 022, Lafayette, MIL 090032, Y 000593 (Section 127-A only), and Y 000802 exhibit weak <001> foliation (Figure 4, Table 2). This weak foliation indicates a lower influence of pure shear (σ, i.e., where $\sigma_1 > \sigma_2 = \sigma_3$). Out of the nakhlites with weaker strength foliations, Caleta el Cobre 022 is the only sample to exhibit no other form of eigenvalue CPO (foliation or lineation), which is consistent with its low J-Index value. Even Lafayette, the section with the next lowest foliation strength, exhibits a weak <010> girdle CPO (Figure 4, Table 2). The lower pure shear component and lack of other CPO present within Caleta el Cobre 022 and Lafayette indicates emplacement in a relatively stagnant magmatic body compared with the other nakhlites. All the other nakhlites exhibit some form of lineation on the <100> (Governador Valadares, MIL 03346, MIL 090030, MIL 090136, Nakhla [USNM 426-1], NWA 10153, Y 000749, Y000802), <100> + <010> (MIL 090032, NWA 998 [T1]), or <010> (Y 000593) lineation in combination with a more dominant <001> foliation (Table 2). The general preference within the nakhlites toward the development of a weaker secondary CPO within the <100> rather than the <010> is inconsistent with most common CPO observed within clinopyroxene-rich igneous rocks on Earth despite plastic deformation within clinopyroxene crystals favoring dislocation along the <001> and <100> (Bascou et al., 2002; Godard & van Roermund, 1995). Even though Y 000593 has a weak lineation, the alignment of <010> over the <100> could indicate different external strain conditions during emplacement compared to the other nakhlites (Bascou et al., 2002). For all but two of the studied nakhlites, the combination of stronger foliation with a weaker lineation suggests a common emplacement mechanism/environment, regardless of whether or not each sample represents an individual flow/intrusion (Corrigan et al., 2015; Daly, Piazolo, et al., 2019; Udry & Day, 2018).

Dominant pure shear (flattening) with a lower component of simple shear (rotational) is commonly associated with gravitationally driven crystal settling, which is the dominant emplacement mechanism in stagnant magma body regimes. Environments where such CPO can develop include intrusions, lava pools and ponds (Iezzi & Ventura, 2002; Merle, 1998), low viscosity slow moving basaltic lavas, or as has been previously suggested for the nakhlites thick lava flows (Friedman Lentz et al., 2011; Treiman, 2005). However, variation (heterogeneity) in CPO strength and the formation of weaker lineation CPO is common within magmatic bodies where pockets of CPO can be highly localized, particularly for bodies associated with a higher discharge volume. In general, greater CPO strengths which tend toward lineation are often observed along the edges of the magmatic body, gravitational settling CPO toward the lower portions (but not the direct base), and random CPO toward the central regions (Nicolas, 1992; Shelley, 1985). Previous CPO analyses of several nakhlites resolved CPO that are consistent with both subaerial flow and stagnant lava lake emplacement environments (Daly, Piazolo, et al., 2019). Results in the present study from a much larger set of nakhlites are consistent with variable emplacement mechanisms and environments. Importantly, they indicate that formation in pure crystal settling environments (e.g., stagnant lava lakes/ponds) may have been less common formation in dynamic flow regimes, be it intrusive or subaerial. In the case of an intrusive emplacement environment, such as a sill or a dyke, stronger CPO with a higher simple shear component is common along the margins but not the central portions of the magma body (Gibb & Henderson, 1992; Komar, 1972; Piazolo et al., 2002; Shelley, 1985). In such a scenario, the low intensity moderate <001> foliations observed among augite crystals could suggest crystal settling via dynamic sorting (Bagnold effect), where each of the nakhlites represents a different axial region from a series of interconnecting dykes or inclined sills (Corrigan et al., 2015; Marsh, 1996) which span at least four separate magmatic events (Cohen et al., 2017). The identification of secondary multiple axes lineations plus the random SPO in most of

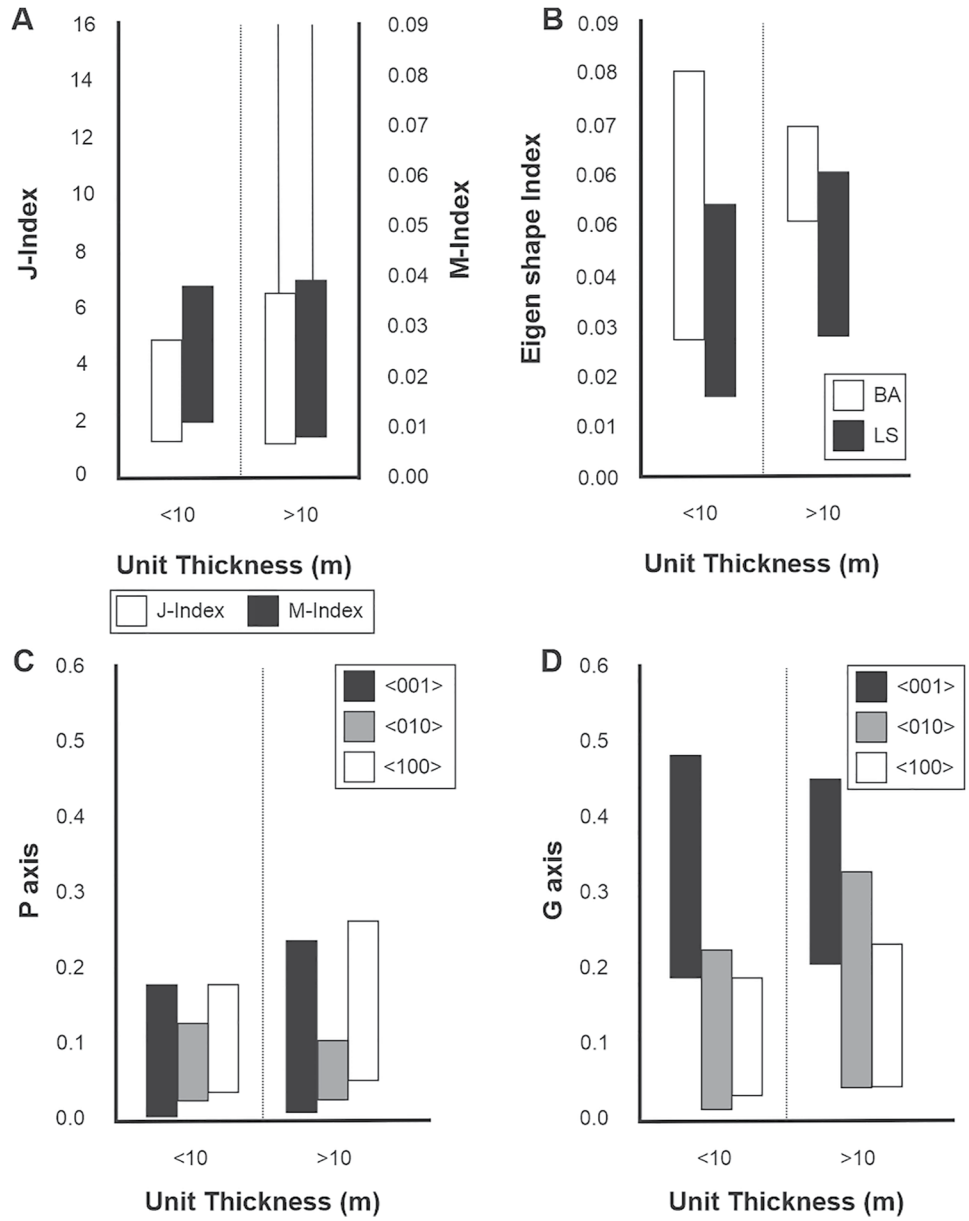

Figure 11. Calculated CPO indices compared against calculated crystal settling magma body unit thickness (Equation 4). (a) J-Index (here defined as low = 1.4–1.8, low-medium 1.8–3.0, medium = 2.4–5.0, medium-strong = 4.0–12.0, and strong >12.0) and M-Index (0 = random 1 = a single crystal); (b) Eigenvalue shape indices which range from 0 to 1 (0 = A or S and 1 = B or L). The BA-Index range for calculated magma bodies is observed to be more restricted for those >10 m; (c) lineation strengths (0.1–0.3 = weak, 0.3–0.5 = moderate, and >0.5 = strong) between the different crystallographic axes; and (d) foliation strengths for the different crystallographic axes (0.1–0.3 = weak, 0.3–0.5 = moderate, and >0.5 = strong). Between the lineation and foliation strengths foliation within the <001> axis is observed to range from weak to moderate, while all other axes show weak to no CPO.

the analyzed samples suggest that the observed <001> foliations have overprinted the initial primary flow CPO within each of the putative nakhlite igneous bodies. During emplacement, such a switch from flow to gravitational crystal settling would account for random SPO, agree with the SPO interpretations of Udry and Day (2018) whilst also maintaining regions of stronger CPO and SPO particularly along the margins of the intrusion (for comparison see Berkley et al., 1980).

4.3. Implications for Understanding the Nakhlite Source Volcano

Igneous rocks, whether formed on Earth or elsewhere in the Solar System, usually show significant mineralogical heterogeneities down to the scale of a few tens of micrometers (Hammer et al., 2010; Jankovics et al., 2012; Kouchi et al., 1986; Lofgren, 1983; Marsh, 2013; Perugini et al., 2003). This characteristic hampers the extrapolation across scales, particularly for meteoritic materials like the nakhlites, of which only millimeter to centimeter-sized fragments are available for in-depth micro-structural analysis. To date, however, significant micro-structural variation within an individual Martian meteorite specimen (325 different meteorite samples as of January 2022) has only been reported for the shergottite Zagami (Becker, 2011). Different conditions on Mars for example, lower gravity, would undoubtedly affect the SPO and CPO expression of Martian magmatic rocks when compared to those formed on Earth. For example, a relatively stronger strain field is required to produce lineation SPO and CPO within a Martian magmatic rock compared with a terrestrial one of the same size, mainly because of the lower gravity on Mars and its subsequent effects on parameters like viscosity, strain, apparent density, and general flow dynamics (Niu & Pang, 2020; Vetere et al., 2019). However, despite the differences between Earth and Mars creating variation in the parameters required to form particular SPO and CPO, the CPO's significance in terms of the general environment of formation are directly comparable. For igneous rocks, increased M-Index and J-Index metric values signal a flow-dominated environment, accounting for increased lineation/simple shear; in PGR analysis, the same is indicated by higher P values. Crystal alignment, which influences CPO development, has been shown to have a number of controls outside of the external strain field (simple shear). The alignment of crystals within an igneous body will be influenced by factors such as the elongate nature of the individual crystals, density and viscosity of the melt, the mineralogical composition and distribution, as well as the surface: volume ratio of the igneous body (Piazolo et al., 2002). CPO heterogeneity between different igneous specimens may be even more pronounced in cases that they formed in multiple events of emplacement (Fenton et al., 2004). Despite the lack of (geological emplacement) context for the nakhlites, the size of each meteorite constrains the maximum relative distance between the replicate sections to centimeter-scale, and the vicinity of the individual meteorites relative to one another to within the area of the currently unknown ejection crater, whose diameter is estimated to be on the scale of kilometers (Artemieva & Ivanov, 2004; Kereszturi & Chatzitheodoridis, 2016).

Coupled emplacement modeling and CPO analysis results demonstrate that the nakhlite specimens analyzed formed via gravity settling dominated crystallization with variable minor components of flow. These results are in agreement with, and expand upon the findings in Daly, Piazolo, et al. (2019) but contradict the findings in Udry and Day (2018), who reported random SPO for 13 nakhlite specimens. The conflicting results in Udry and Day (2018) may be because they used more traditional SPO measurements corrected for slope via measured crystal shape dimensions (rather than proxied SPO via CPO used here). Another option for the reported discrepancy could be from the nakhlites forming under a dynamic sorting regime (Corrigan et al., 2015). An intrusive dyke and sill field could produce the observed random SPO with an aligned CPO via a dynamic sorting regime (Horsman et al., 2005), as reported in Figure 4. In all studied specimens, the percentage of crystallographically aligned phenocrysts within the analysis plane is low (2.53%–10.04%; Table 2). This results in the observable SPO even when accounting for the phenocryst's slope relative to the analysis plane, to appear random in almost all analyzed nakhlite sections even when accounting for the phenocryst's slope relative to the analysis plane (Figure 4). If each section's CPO was not considered, then the data presented in the present study would agree with the interpretations of Udry and Day (2018).

Lastly, it is important to evaluate whether the nakhlite calculated magma body end-member emplacement results can aid in localisation of the nakhlites' origin in the Martian crust. We the authors reiterate that the exact values presented for the end-member mechanisms are not the actual nakhlite unit thicknesses rather they are indicators of end-member viability. Out of the three tested end-member mechanisms pure crystal settling agrees best with observed nakhlite CPO. From this calculation two distinct groups (within the model's current resolution) are identified (Table 3). These two identified groups imply that the nakhlites did not form from a pure crystal settling regime that is, have contributing secondary mechanisms (thermal diffusion and/or crystal convection), or formed in the exact same manner. The proportion between the dominant and secondary mechanisms during emplacement is an area for future work. However, based off physical principals, the current calculated unit thicknesses for the calculated >10 m nakhlites require crystal convection to also be present.

Comparison of the two crystal settling groups against CPO and SPO data, published geochemical data (e.g., Day et al., 2018; Krämer Ruggiu et al., 2020), or age (e.g., Cartwright et al., 2013; Cohen et al., 2017; Krämer Ruggiu

et al., 2020; Mikouchi et al., 2016; Park et al., 2009, 2016) show no identifiable trends or correlations. This observation infers the overall nakhlite data set to be inherently random in terms of both CPO variation, proportion of emplacement mechanisms, and potential magmatic body thicknesses through time (Figures 10 and 11). This heterogeneity of the larger data set could be very easily overlooked when only assessing a subset of the samples. On Earth, individual magmatic events from the same volcano or even multiple lobed flows from a singular event have been observed to shift and evolve in an random manner (e.g., unit thickness, chemical composition, viscosity, CPO, and SPO), particularly when analyzing relatively short periods of a volcano/magma bodies lifespan (Gamble et al., 1999). This intrinsic variability is why field-mapping and high-resolution age dating are critical tools used to understand the evolution of volcanic systems over shorter time periods. Even though the nakhlites have a formation window of at least 93 ± 12 Ma (Cohen et al., 2017) magmatic sources on Mars have been shown to span several billion years (Lapen et al., 2017). In terms of the positioning of the nakhlites, the distal relationship between the samples is limited to the size of their ejection crater on Mars (Cohen et al., 2017; Day et al., 2018; Nyquist et al., 2001; Udry & Day, 2018). Comparison of identified calculated emplacement mechanism groups to published age data showed no observable trends over time which could indicate variable discharge or region of emplacement from the nakhlite magmatic source, or be the result of other factors such as magma viscosity, topography, restriction/spread of the flows/intrusions, etc. (Baumgartner et al., 2017). The resolution of the magma body thicknesses presented here do not yet enable localisation parameters to be fully discerned at a reasonable resolution. However, they do provide a starting point for building more complex models to begin investigating other influential parameters such as, mixing of the end-member emplacement mechanisms calculated here, intrusion versus flow, depth of burial, cooling rate, distance traveled from source etc., which in lieu of field-mapping should assist in narrowing the localized criteria for the nakhlites.

5. Conclusions

The nakhlites have a low intensity weak-medium <001> foliation CPO with all bar two samples exhibiting a weak form of lineation CPO along either one or both of the remaining crystallographic axes. The dominant foliation CPO best agrees with an emplacement mechanism based on crystal settling (e.g., lava ponds, lava lakes, and intrusive sills and dykes). Disparity between observed SPO and CPO across the nakhlites could either be the result of the sections' orientation or an overprinting of initial SPO by the now more dominant CPO <001> foliation. Modelled end-member results for a crystal settling mechanism identifies two distinct groups (outside error) based on calculated unit thickness within nakhlites. The identification of two distinct groups within the nakhlites indicates the presence of secondary emplacement mechanisms contributing to the nakhlites' development. Comparison of the two identified modelled crystal settling groups to presented CPO, SPO, as well as published age and geochemistry data show no correlations or trends. These results highlight the inherent randomness of the large data set, and therefore the source volcanoes discharge through time. However, the nakhlites all exhibit a common dominant emplacement mechanism and CPO, which indicate an overarching first-order characteristic belonging to their source volcano. Overall, this study highlights the importance of assessing larger datasets for investigations into first-order processes, particularly for samples (such as meteorites) where due to the lack of external context, the assessment of limited data can lead to the over-interpretation of local variations.

Data Availability Statement

All data are available at Griffin et al. (2021).

Acknowledgments

The authors are grateful to the following curational facilities for providing the following samples used in this study: NHM London (Governador Valadares), Japanese Antarctic Meteorite Research Centre (NIPR; Y 000593, Y 000749, Y 000802), Macovich Collection, The Museum of Western Australia (Nakhla WAM 12965), Centre Européen de Recherche et d'Enseignemet de Géosciences de l'Environment (CEREGE; Caleta el Cobre 022), the Institute of Meteoritics University of New Mexico (NWA 10153, NWA 12542), Smithsonian (Lafayette, Nakhla USNM 426-1), and ANSMET (MIL 03346, MIL 090030, MIL 090032, and MIL 090136). US Antarctic meteorite samples are recovered by the Antarctic Search for Meteorites (ANSMET) program, which has been funded by the NSF and the NASA, and characterized and curated by the Department of Mineral Sciences of the Smithsonian Institution and Astromaterials Acquisition and Curation Office at NASA Johnson Space Centre. The authors thank the editor Laurent Montési our reviewers Alex Ruzicka and Jon Friedrich as well as David Prior for their helpful comments which significantly enhanced our manuscript. This work was funded by the Science and Technology Facilities Council through grants ST/N000846/1 and ST/H002960/1 to M. R. Lee.

References

Artemieva, N. A., & Ivanov, B. A. (2004). Launch of Martian meteorites in oblique impacts. *Icarus*, *171*(1), 84–101. https://doi.org/10.1016/j.icarus.2004.05.003

Bachmann, F., Hielscher, R., & Schaeben, H. (2011). Grain detection from 2d and 3d EBSD data—Specification of the MTEX algorithm. *Ultramicroscopy*, *111*(12), 1720–1733. https://doi.org/10.1016/j.ultramic.2011.08.002

Bascou, J., Tommansi, A., & Mainprice, D. (2002). Plastic deformation and development of clinopyroxene lattice preferred orientations in eclogites. *Journal of Structural Geology*, *24*(8), 1357–1368. https://doi.org/10.1016/S0191-8141(01)00137-7

Baumgartner, R. J., Baratoux, D., Gaillard, F., & Fiorentini, M. L. (2017). Numerical modelling of erosion and assimilation of sulfur-rich substrate by Martian lava flows: Implications for the genesis of massive sulfide mineralization on Mars. *Icarus*, *296*, 257–274. https://doi.org/10.1016/j.icarus.2017.06.016

Becker, T. E. (2011). *Preferred orientations of pyroxene in the Zagami shergottite: Implications for magmatic emplacement*. Colby College.

Berkley, J. L., Keil, K., & Prinz, M. (1980). Comparative petrology and origin of Governador Valadares and other nakhlites. *Proceedings of Lunar and Planetary Science*, *11*, 1089–1102. Retrieved from https://adsabs.harvard.edu/pdf/1980LPSC…11.1089B

Bestmann, M., & Prior, D. J. (2003). Intragranular dynamic recrystallization in naturally deformed calcite marble: Diffusion accommodated grain boundary sliding as a result of subgrain rotation recrystallization. *Journal of Structural Geology*, *25*(10), 1597–1613. https://doi.org/10.1016/S0191-8141(03)00006-3

Bickel, C. E. (1979). The CIPW normative calculation. *Journal of Geological Education*, *27*(2), 80–82. https://doi.org/10.5408/0022-1368-27.2.80

Bunge, H.-J. (1982). *Texture analysis in materials science: Mathematical methods* (In H.-J. Bunge (Ed.), Paperback). Cuvillier Verlag. https://doi.org/10.7312/chi-18840-001

Callot, J. P., & Guichet, X. (2003). Rock texture and magnetic lineation in dykes: A simple analytical model. *Tectonophysics*, *366*(3–4), 207–222. https://doi.org/10.1016/S0040-1951(03)00096-9

Carr, M. H., & Head, J. W. (2010). Geologic history of Mars. *Earth and Planetary Science Letters*, *294*(3–4), 185–203. https://doi.org/10.1016/j.epsl.2009.06.042

Cartwright, J. A., Gilmour, J. D., & Burgess, R. (2013). Martian fluid and Martian weathering signatures identified in Nakhla, NWA 998 and MIL 03346 by halogen and noble gas analysis. *Geochimica et Cosmochimica Acta*, *105*, 255–293. https://doi.org/10.1016/j.gca.2012.11.046

Cohen, B. E., Mark, D. F., Cassata, W. S., Lee, M. R., Tomkinson, T., Smith, C. L., et al. (2017). Taking the pulse of Mars via dating of a plume-fed volcano. *Nature Communications*, *8*(1), 640. https://doi.org/10.1038/s41467-017-00513-8

Corrigan, C. M., Velbel, M. A., & Vicenzi, E. P. (2015). Modal abundances of pyroxene, olivine, and mesostasis in nakhlites: Heterogeneity, variation, and implications for nakhlite emplacement. *Meteoritics & Planetary Sciences*, *50*(9), 1497–1511. https://doi.org/10.1111/maps.12492

Daly, L., Lee, M. R., Piazolo, S., Griffin, S., Bazargan, M., Campanale, F., et al. (2019). Boom Boom Pow: Shock-facilitated aqueous alteration and evidence for two shock events in the Martian nakhlite meteorites. *Science Advances*, *5*(9), 1–11. https://doi.org/10.1126/sciadv.aaw5549

Daly, L., Piazolo, S., Lee, M. R., Griffin, S., Chung, P., Campanale, F., et al. (2019). Understanding the emplacement of Martian volcanic rocks using petrofabrics of the nakhlite meteorites. *Earth and Planetary Science Letters*, *520*, 220–230. https://doi.org/10.1016/j.epsl.2019.05.050

Day, J. M. D., Tait, K. T., Udry, A., Moynier, F., Liu, Y., & Neal, C. R. (2018). Martian magmatism from plume metasomatized mantle. *Nature Communications*, *9*(1), 4799. https://doi.org/10.1038/s41467-018-07191-0

Durham, W. B., Mirkovich, V. V., & Heard, H. C. (1987). Thermal diffusivity of igneous rocks at elevated pressure and temperature. *Journal of Geophysical Research*, *92*(B11), 11615–11634. https://doi.org/10.1029/jb092ib11p11615

Fenton, C. R., Poreda, R. J., Nash, B. P., Webb, R. H., & Cerling, T. E. (2004). Geochemical discrimination of five Pleistocene lava-dam outburst-flood deposits, western Grand Canyon, Arizona. *The Journal of Geology*, *112*(1), 91–110. https://doi.org/10.1086/379694

Forman, L. V., Bland, P. A., Timms, N. E., Collins, G. S., Davison, T. M., Ciesla, F. J., et al. (2016). Hidden secrets of deformation: Impact-induced compaction within a CV chondrite. *Earth and Planetary Science Letters*, *452*, 133–145. https://doi.org/10.1016/j.epsl.2016.07.050

Forman, L. V., Timms, N. E., Bland, P. A., Daly, L., Benedix, G. K., & Trimby, P. W. (2019). A morphologic and crystallographic comparison of CV chondrite matrices. *Meteoritics & Planetary Sciences*, *2651*(11), 2633–2651. https://doi.org/10.1111/maps.13380

Frets, E., Tommasi, A., Garrido, C. J., Padrón-Navarta, J. A., Amri, I., & Targuisti, K. (2012). Deformation processes and rheology of pyroxenites under lithospheric mantle conditions. *Journal of Structural Geology*, *39*, 138–157. https://doi.org/10.1016/j.jsg.2012.02.019

Friedman Lentz, R. C., McCoy, T. J., Collins, L. E., Corrigan, C. M., Benedix, G. K., Taylor, G., & Harvey, R. (2011). Theo's flow, Ontario, Canada: A terrestrial analog for Martian meteorites. *Geological Society of America Special Paper*, *483*, 263–277. https://doi.org/10.1130/2011.2483(17)

Gamble, J. A., Wood, C. P., Price, R. C., Smith, I. E. M., Stewart, R. B., & Waight, T. (1999). A fifty-year perspective of magmatic evolution on Ruapehu Volcano, New Zealand: Verification of open system behaviour in an arc volcano. *Earth and Planetary Science Letters*, *170*(3), 301–314. https://doi.org/10.1016/S0012-821X(99)00106-5

Gerth, D., & Schwarzer, R. A. (1993). Graphical representation of grain and Hillock orientations in annealed Al–1% Si films. *Textures and Microstructures*, *21*(2–3), 177–193. https://doi.org/10.1155/tsm.21.177

Gibb, F. G. F., & Henderson, C. M. B. (1992). Convection and crystalisation in sills. *Contributions to Mineralogy and Petrology*, *109*(4), 538–545. https://doi.org/10.1007/BF00306555

Godard, G., & Van Roermund, H. L. M. (1995). Deformation-induced clinopyroxene fabrics from eclogites. *Journal of Structural Geology*, *17*(10), 1425–1443. https://doi.org/10.1016/0191-8141(95)00038-F

Greeley, R., & Spudis, P. D. (1981). Volcanism on Mars. *Reviews of Geophysics and Space Physics*, *19*(1), 13–41. https://doi.org/10.1029/RG019i001p00013

Griffin, S., Daly, L., Keller, T., Piazolo, S., Forman, L. V., Lee, M. R., et al. (2021). Constraints on the emplacement of Martian nakhlite igneous rocks and their source volcano from advanced micro-petrofabric analysis (Version MTEX 5.7.0, MATLAB 2021a) [Dataset]. Zenodo. https://doi.org/10.5281/ZENODO.5545821

Grott, M., Baratoux, D., Hauber, E., Sautter, V., Mustard, J., Gasnault, O., et al. (2013). Long-term evolution of the Martian crust-mantle system. *Space Science Reviews*, *174*(1–4), 49–111. https://doi.org/10.1007/s11214-012-9948-3

Hammer, J. E., Sharp, T. G., & Wessel, P. (2010). Heterogeneous nucleation and epitaxial crystal growth of magmatic minerals. *Geology*, *38*(4), 367–370. https://doi.org/10.1130/G30601.1

Henry, H., Tilhac, R., Griffin, W. L., O'Reilly, S. Y., Satsukawa, T., Kaczmarek, M.-A., et al. (2017). Deformation of mantle pyroxenites provides clues to geodynamic processes in subduction zones: Case study of the Cabo Ortegal Complex, Spain. *Earth and Planetary Science Letters*, *472*, 174–185. https://doi.org/10.1016/j.epsl.2017.05.028

Hidas, K., Garrido, C. J., Booth-Rea, G., Marchesi, C., Bodinier, J. L., Dautria, J. M., et al. (2019). Lithosphere tearing along STEP faults and synkinematic formation of lherzolite and wehrlite in the shallow subcontinental mantle. *Solid Earth*, *10*(4), 1099–1121. https://doi.org/10.5194/se-10-1099-2019

Horsman, E., Tikoff, B., & Morgan, S. (2005). Emplacement-related fabric and multiple sheets in the Maiden Creek sill, Henry Mountains, Utah, USA. *Journal of Structural Geology*, *27*(8), 1426–1444. https://doi.org/10.1016/j.jsg.2005.03.003

Hunter, R. H. (1996). Texture development in cumulate rocks. *Developments in Petrology*, *15*(C), 77–101. https://doi.org/10.1016/S0167-2894(96)80005-4

Iezzi, G., & Ventura, G. (2002). Crystal fabric evolution in lava flows: Results from numerical simulations. *Earth and Planetary Science Letters*, *200*(1–2), 33–46. https://doi.org/10.1016/S0012-821X(02)00617-9

Ismaïl, W. B., & Mainprice, D. (1998). An olivine fabric database: An overview of upper mantle fabrics and seismic anisotropy. *Tectonophysics*, *296*(1–2), 145–157. https://doi.org/10.1016/S0040-1951(98)00141-3

Jankovics, M. É., Harangi, S., Kiss, B., & Ntaflos, T. (2012). Open-system evolution of the Füzes-tó alkaline basaltic magma, western Pannonian Basin: Constraints from mineral textures and compositions. *Lithos*, *140–141*, 25–37. https://doi.org/10.1016/j.lithos.2012.01.020

Jerram, D. A., Dobson, K. J., Morgan, D. J., & Pankhurst, M. J. (2018). The petrogenesis of magmatic systems: Using igneous textures to understand magmatic processes. In S. Burchardt (Ed.), *Volcanic and igneous plumbing systems: Understanding magma transport, storage, and evolution in the Earth's crust* (pp. 191–229). Elsevier. https://doi.org/10.1016/B978-0-12-809749-6.00008-X

Kalidindi, S. R., Knezevic, M., Niezgoda, S., & Shaffer, J. (2009). Representation of the orientation distribution function and computation of first-order elastic properties closures using discrete Fourier transforms. *Acta Materialia*, *57*(13), 3916–3923. https://doi.org/10.1016/j.actamat.2009.04.055

Kereszturi, A., & Chatzitheodoridis, E. (2016). Searching for the source crater of nakhlite meteorites. *Origins of Life and Evolution of the Biosphere*, *46*(4), 455–471. https://doi.org/10.1007/s11084-016-9498-x

Komar, P. D. (1972). Interactions of phenocrysts and flow differentiation of igneous dikes and sills. *The Geological Society of America Bulletin*, *83*(4), 973–988. https://doi.org/10.1130/0016-7606(1972)83[973:MIOPAF]2.0.CO;2

Kouchi, A., Tsuchiyama, A., & Sunagawa, I. (1986). Effect of stirring on crystallization kinetics of basalt: Texture and element partitioning. *Contributions to Mineralogy and Petrology*, *93*(4), 429–438. https://doi.org/10.1007/BF00371713

Krämer Ruggiu, L., Gattacceca, J., Bevouard, B., Udry, A., Debaille, V., Rochette, P., et al. (2020). Caleta el Cobre 022 Martian meteorite: Increasing nakhlite diversity. *Meteoritics & Planetary Sciences*, *25*(7), 1–25. https://doi.org/10.1111/maps.13534

Kurokawa, H., Sato, M., Ushioda, M., Matsuyama, T., Moriwaki, R., Dohm, J. M., & Usui, T. (2014). Evolution of water reservoirs on Mars: Constraints from hydrogen isotopes in Martian meteorites. *Earth and Planetary Science Letters*, *394*, 179–185. https://doi.org/10.1016/j.epsl.2014.03.027

Lapen, T. J., Righter, M., Andreasen, R., Irving, A. J., Satkoski, A. M., Beard, B. L., et al. (2017). Two billion years of magmatism recorded from a single Mars meteorite ejection site. *Science Advances*, *3*(2), 1–7. https://doi.org/10.1126/sciadv.1600922

Lapen, T. J., Righter, M., Brandon, A. D., Debaille, V., Beard, B. L., Shafer, J. T., & Peslier, A. H. (2010). A younger age for ALH 84001 and its geochemical link to shergottite sources in Mars. *Science*, *328*(April), 347–352. https://doi.org/10.1126/science.1185395

Lee, M. R., Daly, L., Cohen, B. E., Hallis, L. J., Griffin, S., Boyce, A. J., & Mark, D. F. (2018). Aqueous alteration of the Martian meteorite Northwest Africa 817: Probing fluid – Rock interaction at the nakhlite launch site. *Meteoritics & Planetary Sciences*, *53*(11), 2395–2412. https://doi.org/10.1111/maps.13136

Lofgren, G. E. (1983). Effect of heterogeneous nucleation on basaltic textures: A dynamic crystallization study. *Journal of Petrology*, *24*(3), 229–255. https://doi.org/10.1093/petrology/24.3.229

Mainprice, D., Bachmann, F., Hielscher, R., & Schaeben, H. (2015). Descriptive tools for the analysis of texture projects with large datasets using MTEX: Strength, symmetry and components. *Geological Society – Special Publications*, *409*(1), 251–271. https://doi.org/10.1144/SP409.8

Marsh, B. D. (1996). Solidification fronts and magmatic evolution. *Mineralogical Magazine*, *60*(398), 5–40. https://doi.org/10.1180/minmag.1996.060.398.03

Marsh, B. D. (2013). On some fundamentals of igneous petrology. *Contributions to Mineralogy and Petrology*, *166*(3), 665–690. https://doi.org/10.1007/s00410-013-0892-3

McBirney, A. R. (1993). *Igneous petrology* (2nd ed.), Jones and Barltett Publishers.

McSween, H. Y., Grove, T. L., Friedman Lentz, R. C., Dann, J. C., Holzheid, A. H., Riciputi, L. R., & Ryan, J. G. (2001). Geochemical evidence for magmatic water within Mars from pyroxenes in the shergotty meteorite. *Nature*, *409*(6819), 487–490. https://doi.org/10.1038/35054011

McSween, H. Y., & Treiman, A. H. (1998). Martian Meteroties. In J. J. Papike (Ed.), *Planetary materials*, *Reviews in Mineralogy* (Vol. 36, pp. 1–53). Mineralogical Society America.

Merle, O. (1998). Internal strain within lava flows from analogue modelling. *Journal of Volcanology and Geothermal Research*, *81*(3–4), 189–206. https://doi.org/10.1016/S0377-0273(98)00009-2

Mikouchi, T., Righter, M., Ziegler, K., & Irving, A. J. (2016). Petrology, mineralogy and oxygen isotopic composition of the Northwest Africa 10153 nakhlite: A sample from a different flow from other nakhlites? In *79th Annual Meeting of the Meteoritical Society* (p. A6396). https://doi.org/10.1111/maps.12934

Nicolas, A. (1992). Kinematics in magmatic rocks with special reference to gabbros. *Journal of Petrology*, *33*(4), 891–915. https://doi.org/10.1093/petrology/33.4.891

Niu, R., & Pang, M. (2020). Numerical study on the effect of gravity levels on apparent viscosity of bubbly suspensions. *Microgravity Science and Technology*, *32*(4), 555–577. https://doi.org/10.1007/s12217-020-09792-1

Nyquist, L. E., Bogard, D. D., Shih, C. Y., Greshake, A., Stöffler, D., & Eugster, O. (2001). Ages and geologic histories of Martian meteorites. In R.Kallenbach, J.Geiss, & W. K.Hartmann (Eds.), *Chronology and evolution of Mars*. *Space Sciences Series of ISSI* (Vol. 12, pp. 105–164). Springer. https://doi.org/10.1007/978-94-017-1035-0_5

Park, J., Garrison, D. H., & Bogard, D. D. (2009). ^{39}Ar-^{40}Ar ages of Martian nakhlites. *Geochimica et Cosmochimica Acta*, *73*(7), 2177–2189. https://doi.org/10.1016/j.gca.2008.12.027

Park, J., Nyquist, L. E., Herzog, G. F., Turrin, B. D., Linsay, F. N., Delaney, J. S., & Swisher, C. C., III. (2016). ^{40}Ar/^{39}Ar ages of nakhlites Miller Range (MIL) 090030, 090032 and 090136. In *Lunar and Planetary Science Conference XCVII* (pp. 1821–1822). https://doi.org/10.1029/2009GC003013

Paterson, S. R., Fowler, T. K., Schmidt, K. L., Yoshinobu, A. S., Yuan, E. S., & Miller, R. B. (1998). Interpreting magmatic fabric patterns in plutons. *Lithos*, *44*(1–2), 53–82. https://doi.org/10.1016/S0024-4937(98)00022-X

Perugini, D., Busà, T., Poli, G., & Nazzareni, S. (2003). The role of chaotic dynamics and flow fields in the development of disequilibrium textures in volcanic rocks. *Journal of Petrology*, *44*(4), 733–756. https://doi.org/10.1093/petrology/44.4.733

Piazolo, S., Bons, P. D., & Passchier, C. W. (2002). The influence of matrix rheology and vorticity on fabric development of populations of rigid objects during plane strain deformation. *Tectonophysics*, *351*(4), 315–329. https://doi.org/10.1016/S0040-1951(02)00220-2

Pruseth, K. L. (2009). Calculation of the CIPW norm: New formulas. *Journal of Earth System Science*, *118*(1), 101–113. https://doi.org/10.1007/s12040-009-0010-0

Ruzicka, A. M., & Hugo, R. C. (2018). Electron backscatter diffraction (EBSD) study of seven heavily metamorphosed chondrites: Deformation systematics and variations in pre-shock temperature and post-shock annealing. *Geochimica et Cosmochimica Acta*, *234*, 115–147. https://doi.org/10.1016/j.gca.2018.05.014

Shelley, D. (1985). Determining paleo-flow directions from groundmass fabrics in the Lyttelton radial dykes, New Zealand. *Journal of Volcanology and Geothermal Research*, *25*(1–2), 69–79. https://doi.org/10.1111/ane.12608

Skemer, P., Katayama, I., Jiang, Z., & Karato, S. I. (2005). The misorientation index: Development of a new method for calculating the strength of lattice-preferred orientation. *Tectonophysics*, *411*(1–4), 157–167. https://doi.org/10.1016/j.tecto.2005.08.023

Taylor, G. J. (2013). The bulk composition of Mars. *Chemie Der Erde – Geochemistry*, *73*(4), 401–420. https://doi.org/10.1016/j.chemer.2013.09.006

Treiman, A. H. (2005). The nakhlite meteorites: Augite-rich igneous rocks from Mars. *Chemie Der Erde – Geochemistry*, *65*(3), 203–270. https://doi.org/10.1016/j.chemer.2005.01.004

Udry, A., & Day, J. M. D. (2018). 1.34 billion-year-old magmatism on Mars evaluated from the co-genetic nakhlite and chassignite meteorites. *Geochimica et Cosmochimica Acta*, *238*, 292–315. https://doi.org/10.1016/J.GCA.2018.07.006

Udry, A., Howarth, G. H., Herd, C., Day, J. M. D., Lapen, T. J., & Filiberto, J. (2020). What Martian meteorites reveal about the interior and surface of Mars. *Journal of Geophysical Research: Planets*, *125*(12), e2020JE006523. https://doi.org/10.1029/2020JE006523

Van Der Werf, T., Chatzaras, V., Marcel Kriegsman, L., Kronenberg, A., Tikoff, B., & Drury, M. R. (2017). Constraints on the rheology of the lower crust in a strike-slip plate boundary: Evidence from the San Quintín xenoliths, Baja California, Mexico. *Solid Earth*, *8*(6), 1211–1239. https://doi.org/10.5194/se-8-1211-2017

Vetere, F., Murri, M., Alvaro, M., Domeneghetti, M. C., Rossi, S., Pisello, A., et al. (2019). Viscosity of pyroxenite melt and its evolution during cooling. *Journal of Geophysical Research: Planets*, *124*(5), 1451–1469. https://doi.org/10.1029/2018JE005851

Vollmer, F. W. (1990). An application of eigenvalue methods to structural domain analysis. *Bulletin of the Geological Society of America*, *102*(6), 786–791. https://doi.org/10.1130/0016-7606(1990)102<0786:AAOEMT>2.3.CO;2

Watt, L. E., Bland, P. A., Prior, D. J., & Russell, S. S. (2006). Fabric analysis of Allende matrix using EBSD. *Meteoritics & Planetary Sciences*, *41*(7), 989–1001. https://doi.org/10.1111/j.1945-5100.2006.tb00499.x

Werner, S. C. (2009). The global Martian volcanic evolutionary history. *Icarus*, *201*(1), 44–68. https://doi.org/10.1016/j.icarus.2008.12.019

Zuber, M. T. (2001). The crust and mantle of Mars. *Nature*, *412*(6843), 220–227. https://doi.org/10.1038/35084163